

# A Multi-Wavelength Study of Star Formation in 15 Local Star-Forming Galaxies

Madison V. Smith,<sup>1</sup><sup>\*</sup> L. van Zee<sup>1</sup>, S. Salim<sup>1</sup>, D. Dale<sup>2</sup>, S. Staudaher<sup>3</sup>,  
T. Wrock<sup>1</sup>, A. Maben<sup>1</sup>

<sup>1</sup>*Department of Astronomy, Indiana University, Bloomington IN, USA*

<sup>2</sup>*Department of Physics & Astronomy, University of Wyoming, Laramie WY, USA*

<sup>3</sup>*College of Osteopathic Medicine, Sam Houston State University, Conroe TX, USA*

Accepted XXX. Received YYY; in original form ZZZ

## ABSTRACT

We have fit the far-ultraviolet (FUV) to mid-infrared (MIR) spectral energy distributions (SEDs) for several nearby galaxies (< 20 Mpc). Global, radial, and local photometric measurements are explored to better understand how SED-derived star formation histories (SFHs) and classic star formation rate (SFR) tracers manifest at different scales. Surface brightness profiles and radial SED fitting provide insight into stellar population gradients in stellar discs and haloes. A double exponential SFH model is used in the SED fitting to better understand the distributions of young vs. old populations throughout these galaxies. Different regions of a galaxy often have undergone very different SFHs, either in strength, rate, timing, or some combination of all these factors. An analysis of individual stellar complexes within these galaxies shows a relationship between the ages of stellar clusters and how these clusters are distributed throughout the galaxy. These star formation properties are presented alongside previously published HI observations to provide a holistic picture of a small sample of nearby star-forming galaxies. The results presented here show that there is a wide variety of star formation gradients and average stellar age distributions that can manifest in a  $\Lambda$ CDM universe.

**Key words:** galaxies: star formation – galaxies: evolution – galaxies: fundamental parameters

## 1 INTRODUCTION

The way a galaxy evolves is inherently dependent on the laws of structure formation in the universe. In particular,  $\Lambda$ CDM models support the theory that galaxies form "inside-out", meaning that there is an expectation that the edges of stellar discs are to be richer in young, metal-poor stars than the inner regions (e.g., Abadi et al. 2003; Aumer et al. 2013). The color gradients of many spiral galaxies have corroborated these models by showing a trend of red to blue colors as a function of galactocentric distance (e.g., de Jong 1996; MacArthur et al. 2004). Beyond the stellar disc, the stellar halo can be simulated as a build up of past major/minor merger and accretion events (e.g., Alberts et al. 2011; D’Souza et al. 2014) or as stars undergoing stellar migration (Sellwood & Binney 2002), both allowing the edges of a galaxy to contain older populations. While dwarf galaxies also show older stellar populations at larger radii, this population gradient may be better explained by stellar migration (e.g., Zhang et al. 2012; El-Badry et al. 2016). Simulations wishing to recreate accurate evolutionary models should be validated by an extensive catalogue of the star formation properties and the stellar population distributions of real galaxies. This project is the first step in providing those details for several nearby galaxies, so as to

enumerate the possible outcomes of the complex process of galaxy evolution.

A popular technique in constraining a galaxy’s components and physical properties is spectral energy distribution (SED) fitting. Multi-wavelength photometry is matched to libraries of SEDs made from convolutions of stellar synthesis models, dust attenuation curves, and more to infer details about the physical properties of a galaxy (e.g.; Larson & Tinsley 1978; Hunt et al. 2019). A wide variety of physical properties, such as total mass, dust attenuation, and metallicity, can be inferred from the best-fitting modelled SED. Of interest for this project, SED fitting can give insight into a galaxy’s star formation history (SFH) both on global and spatially-resolved scales (e.g., Reddy et al. 2012; Mentuch Cooper et al. 2012; Dale et al. 2016, 2020). Combining the results of the model fitting with commonly used SFR tracers, such as the FUV+24 $\mu$ m flux, can provide a more comprehensive look at the variety of current and past star formation histories possible for nearby star-forming galaxies. Previous HI observations are also presented alongside these photometric results to enhance the discussion on the current and past evolutionary steps these galaxies are experiencing, even though the HI is not used in the SED fitting. In particular, HI surface density maps and velocity fields deepen our understanding of the immediate environment around and the varying kinematics within these galaxies (e.g., Swaters et al. 2002; Holwerda et al. 2012).

<sup>\*</sup> E-mail: madvsm@iu.edu

In addition to the multiwavelength approach, this project also looks at star formation properties on different spatial scales because the interpretation of a galaxy's properties may be methodology- and scale-dependent (Kennicutt & Evans 2012). Measuring a galaxy's global star formation properties is a method for classifying whether that galaxy is star-forming or quiescent (Noeske et al. 2007). While the global properties of galaxies are important to know, nearby galaxies, especially those in the Local Volume, can be observed with more detail. Especially in the case of spirals, a radial analysis of the star formation properties in a galaxy can give more detailed information about where individual stellar populations tend to reside (e.g., Muñoz-Mateos et al. 2011; Monachesi et al. 2013). The EDGES Survey (van Zee et al. 2012; Staudaher et al. 2019), the source of the NIR measurements used here, was able to detect the low-surface brightness, extended stellar haloes that serve as evidence for hierarchical evolution (Bullock & Johnston 2005; Cooper et al. 2013).

On a smaller scale than simply looking at radial trends, tracing and analyzing individual stellar complexes throughout the disc can be enlightening as to how star formation persists in different environments. Thilker et al. (2005) showed the existence of moderately young stellar clusters in the outer, low-density regions of M83, furthering the argument that star formation thresholds fall short of describing the ability of star formation to take place in specific areas of a galaxy. Continuing the studies of Thilker et al. (2005) and others (e.g., Alberts et al. 2011; Barnes et al. 2014), this project will look at the properties of UV-selected stellar clusters in our sample of local galaxies. A combination of SED-fitting and clustering algorithms is used to look at the characteristic separation of young stellar complexes depending on their age. With global, radial, and local star formation properties presented in one place, this project aims to catalogue the abundance of star formation properties that can be produced in a  $\Lambda$ CDM universe.

Section 2 details the sources of the measured images and gives an overview of the sample. Section 3 explains the methods used in this analysis. Section 4 presents the main results. Section 5 provides more context for these results, including a comparison of these SED-derived SFH results to past CMD-derived results for several galaxies. Section 6 summarizes the major conclusions for this project, and discusses possible future avenues of research. Appendix A presents the individual analysis of the photometric measurements and radial SFHs for each galaxy, including information about each galaxy in the literature. Appendix A also presents the HI distributions of these galaxies, making it possible in some cases to draw more distinct conclusions about the evolutionary path the galaxy may be on.

## 2 OBSERVATIONS AND SAMPLE

This analysis of 15 galaxies relies on multiwavelength observations gathered from archival GALEX and *Spitzer* data, as well as optical observations published here for the first time. Because this subsample is selected from the EDGES sample (van Zee et al. 2012), exceptionally deep 3.6 and 4.5  $\mu$ m *Spitzer* Infrared Array Camera (IRAC) (Fazio et al. 2004) images are available. For more coverage in the mid-IR, 5.8, 8.0, and 24  $\mu$ m images from either SINGS (Kennicutt et al. 2003) or the LVL Survey (Dale et al. 2009) are used in our measurements. The observing strategy outlined for both surveys made it such that there was a net integration time of 240s (160s) for each pixel in the mosaicked IRAC (MIPS) images. Table 1 shows the integration times for the GALEX images and the sources of these supplementary IR observations used in this analysis.

The campaign to observe the EDGES galaxies in the optical, including narrowband  $H\alpha$  observations, at the WIYN 0.9m on Kitt

**Table 1.** UV integration times (in seconds) and the survey where the UV and IR images were published. Sources for the IR images : (1) Kennicutt et al. (2003), (2) Dale et al. (2009). <sup>a</sup> Optical images for NGC 7793 were also from Kennicutt et al. (2003).

Galaxy	FUV	NUV	Source
NGC 0024	1577	1577	(1)
NGC 3344	895	1400	(2)
NGC 3486	1488	3072	(2)
NGC 3938	-	3045	(1)
NGC 4068	1350	2281	(2)
NGC 4096	1650	1650	(2)
NGC 4214	1066	2006	(2)
NGC 4242	1683	3282	(2)
NGC 4618	1630	3259	(2)
NGC 4625	1630	3259	(2)
NGC 7793 <sup>a</sup>	1553	1553	(1)
UGC 07408	1450	2691	(2)
UGC 07577	1684	1684	(2)
UGC 07608	1684	1684	(2)
UGC 08320	1584	3116	(2)

Peak gives this project the opportunity to incorporate more multi-wavelength measurements in the SED fitting. The narrowband  $H\alpha$  measurements were included in the SED fitting. It is important to note, however, not all of the  $H\alpha$  flux can be attributed to the ionizing radiation of O stars. All  $H\alpha$  flux within an annulus is averaged for the radial analysis component of this project. This makes the EW( $H\alpha$ ) profiles more difficult to interpret in the context of star formation, but they are still included in the data presentation. In all cases, the B and R observations have been used in the methods outlined in Section 3. For some galaxies, the full UVBR coverage is available and was included in the methodology. These optical images were observed with either S2KB or HDI on the WIYN 0.9m telescope between May 25, 2009 and April 19, 2018. Typical integration times for the U, B, V, R, and  $H\alpha$  single exposures are 1200, 900, 600, 300, and 1200s respectively. In all cases, the final science images utilized for this project were combinations of at least two individual exposures for each filter. The integration times and NCOMBINE procedure ensured that the observations at optical wavelengths were not the limiting factor when measuring low surface brightness regions of the galaxies. The surface brightness limit for the B measurements is  $\sim 26.5$  mag arcsec<sup>-2</sup>.

Some properties of our sample are given in Table 2, including morphology, distances, and Galactic reddening ( $A_V$ ). All 15 galaxies are within 20 Mpc, but span a wide range of morphologies, inclination, and luminosity. This sample is the first in a series of papers to look at the star formation in local galaxies using the methods outlined in Section 3. Another important aspect in understanding these galaxies can be studied by looking at their HI distributions. HI gas plays an important role in the regulation of star formation in galaxies (e.g., van Zee et al. 1997); therefore, the HI surface density and velocity fields are presented in conjunction with the SED fitting and photometric measurements. The HI observations come from a variety of sources. These sources and cursory analysis of the HI distributions in the galaxies are discussed in Appendix A.

## 3 METHODS

The surface brightness profiles are measured using the `ellipse` package in IRAF. Images were cleaned such that any foreground or

**Table 2.** Sources for distances: (1) Tully et al. (2013), (2) Tully et al. (2016), (3) Poznanski et al. (2009), (4) Jacobs et al. (2009), (5) Sorce et al. (2014), (6) McQuinn et al. (2017), (7) Zgirski et al. (2017), (8) Tully & Fisher (1988). All information is taken from the NASA/IPAC Extragalactic Database (NED).

Galaxy	Morphology	$A_V$	$cz$ (km s <sup>-1</sup> )	d (Mpc)
NGC 0024	SA(s)c	0.053	555	7.7 (1)
NGC 3344	(R)SAB(r)bc	0.091	582	9.8 (1)
NGC 3486	SAB(r)c	0.059	681	12.6 (2)
NGC 3938	SA(s)c HII	0.058	810	17.9 (3)
NGC 4068	IAm	0.059	210	4.4 (4)
NGC 4096	SAB(rs)c	0.050	567	12.4 (1)
NGC 4214	IAB(s)m	0.060	291	2.9 (1)
NGC 4242	SAB(s)dm	0.033	507	5.2 (5)
NGC 4618	SB(rs)m HII	0.058	543	6.5 (2)
NGC 4625	SAB(rs)m pec	0.50	621	11.8 (6)
NGC 7793	SA(s)d HII	0.053	231	3.4 (7)
UGC 07408	IAm	0.032	462	7.3 (1)
UGC 07577	Im	0.056	195	2.6 (1)
UGC 07608	Im	0.047	537	7.6 (8)
UGC 08320	IBm	0.042	192	4.3 (1)

background sources were removed. Any of these sources directly on a galaxy were interpolated over, instead of having the pixel values simply set to zero. Interpolating over the sources helped to preserve the flux of these galaxies especially in the case of bright foreground stars. Families of ellipses were grown inward and outward with characteristics (ellipticity, position angle, etc.) drawn from the properties of the isophotal ellipse at  $R_{25}$ , which is the radius at which the average surface brightness in the B band is 25 mag arcsec<sup>-2</sup>. The growth of these ellipses is logarithmic with a multiplicative factor of 1.1 to ensure adequate signal to noise even in the far edges of the galaxy. The smallest of the ellipses (the inner annulus) was never smaller than the highest resolution limit of all the available images, which is set by the 24 $\mu$ m MIPS images at 6". The annulus-averaged surface magnitude in each ellipse is recorded to create the surface brightness profile according to the best-practice methods of Barnes et al. (2014). These surface magnitudes are inclination corrected, assuming the ellipticity of a galaxy corresponds directly to its inclination. Next, the surface magnitudes are corrected for Galactic extinction (Schlafly & Finkbeiner 2011) assuming  $A_V/E(B-V) \approx 3.1$  and the reddening curve from Fitzpatrick (1999).

It is important to note that the inclination corrections are based on the photometric properties of the isophote at  $R_{25}$ , and do not include effects based on the thickness of the disc. For this correction,  $\cos i = b/a$ , where  $b/a$  is the axial ratio of the minor to the major axis. This interpretation is used even in the case of dwarf galaxies where inclination angle may not be well-defined, for consistency. On a similar consistency note, often concentric ellipses are not the most intuitive method of exploring a surface brightness profile, but this method is consistently used across the sample even in the case of highly-irregular or clumpy galaxies. While there are more precise formulations of the inclination correction, the simple  $\cos i$  correction can be used consistently across many morphologies. The simplicity of using the ellipse parameters ( $b/a$ ) to define the inclination of a galaxy does not affect the results presented in the project.

While this logarithmic growth of the ellipses allows for finely-spaced, consistent coverage of each galaxy, it creates a large amount of concentric regions ( $\sim 30$  per galaxy) to be fed into CIGALE<sup>1</sup>

(Noll et al. 2009; Boquien et al. 2019) that then need to be analysed independently. In the interest of being able to effectively analyse the trends across a galaxy without being overwhelmed by the regions of interest, the above method is used only to show the surface brightness and color profiles. For the SED-fitting, a slightly different method is used for clarity in the analysis. The preliminary photometry provides the details needed to calculate the total light from a galaxy using its asymptotic magnitude derived from the curve of growth (Cairós et al. 2001). The total magnitude of the galaxy is then used to find the half-light radius.

Using the same centre, ellipticity, and position angle from the  $R_{25}$  analysis, but with the half light radius as the parent ellipse's semi-major axis, a new family of ellipses is grown. These ellipses are grown by a factor of 1.8 such that there are three regions interior and two to four regions exterior to the half light radius. The number of exterior regions is dependent on the spatial extent of the disc in all of the bands, allowing for a maximum of seven concentric regions to be measured for any given galaxy. This coarser definition of annuli provides another advantage, besides having fewer regions to analyse. We opted not to smooth the higher resolution images (the optical, 3.6  $\mu$ m, and 4.5  $\mu$ m images) to match the other, lower resolution images. Dale et al. (2016) showed that coarsely placed concentric ellipses lead to consistent results whether or not the higher resolution images are smoothed.

The surface magnitudes created from this method are then inclination corrected and corrected for Galactic extinction (same as before), but are then converted to fluxes (mJy) to be fed into the SED-fitting code, CIGALE. Galactic extinction and redshifts were obtained through the NASA/IPAC Extragalactic Database (NED). This methodology effectively assumes independent evolution of the concentric rings being given to CIGALE, as the SED-fitting is done on each ring without knowledge about the neighboring rings. Although this simplifying assumption does not take into account effects of stellar migration, modeling galaxies as independent rings has been shown to reproduce realistic stellar properties (Boissier & Prantzos 1999, 2000; Muñoz-Mateos et al. 2011).

CIGALE allows for a large parameter space to be explored, but the parameters used for this project are similar to those of Dale et al. (2016) and Dale et al. (2020) in order to model realistic parameters for nearby galaxies. We use the Bruzual & Charlot (2003) library of single stellar populations (SSPs) to model the stellar part of the spectrum. We use the SSPs modelled with the Salpeter (1955) stellar IMF (lower and upper mass cut offs are  $m_L = 0.1M_\odot$  and  $m_U = 100M_\odot$ ) and a range of metallicities (see Table 3). The single parameter dust emission model with no AGN component from Dale et al. (2014) is used as well.

The nebular module, an optional module in CIGALE, was included in the parameter space because the emission-line flux can contribute a significant amount to the broadband fluxes of galaxies with high equivalent widths and sSFRs. Without accounting for emission lines, the SED-derived specific star formation rates (sSFR = SFR / stellar mass) of these already high-sSFR galaxies are overestimated (Salim et al. 2016). Because the galaxies in this sample are already designated as star forming, including the nebular emission in the SEDs produce better fits at UV and optical wavelengths. It has also been shown that gaseous nebular emission can become a major source of flux for young, low-metallicity stellar populations (Anders & Fritze-v. Alvensleben 2003). The dust attenuation curve based on Calzetti et al. (2000) and Leitherer et al. (2002) was used. The exact ranges of values allowed for the SED parameters are given in Table 3.

We opt to use a double exponential SFH for this project. This

<sup>1</sup> Version 2018.0, <https://cigale.lam.fr>

functional form of a SFH involves five parameters. There are two onsets of star formation, starting at times  $t_o$  and  $t_y$  for the older and younger stellar populations, respectively. Both epochs of star formation have exponential decreases in the SFR, which is described by the e-folding times,  $\tau_o$  and  $\tau_y$ . The final parameter related to the double exponential SFH is  $f_{burst}$ , the fraction of stars formed in the younger burst of star formation relative to the total stellar mass formed. We set the age of the older stellar population,  $t_o$  to be 10 Gyr, but allow the e-folding time,  $\tau_o$  to vary, as in Noll et al. (2009). For the more recent burst of star formation, we allow the age  $t_y$ ,  $\tau_y$ , and burst fraction,  $f_{burst}$  to vary. A double exponential SFH is favored over the single exponential because the double exponential has been shown to produce better fits, especially in the case of more complicated, bursty SFHs often associated with low-mass dwarfs (Weisz et al. 2011; Salim et al. 2016).

Setting the older stellar population's age to 10 Gyr and only allowing the newer population to be at most 4 Gyr old forces the stars to be formed in one of two possible formation mechanisms. An older population is expected to be made during the formation and assembly of the galaxy, while a newer population forms during the evolution and current times of the galaxy (McQuinn et al. 2010). Keeping these time-scales separate from one another is also important because any measure of SFH has systematically larger uncertainties on the more ancient SFH than on the recent SFH, so allowing only a single  $t_o$  still captures the essence of ancient star formation without needlessly complicating the modelling process. This SFH template allows for a clear division between older and younger populations, with the focus of this research being on the younger population.

This type of SED fitting requires us to limit our SFH models to a library of functional forms, even though the true SFH of a galaxy is likely to be more complicated. Parametric models have been shown to produce biases and incorrect uncertainties for output physical parameters. The use of nonparametric models have been used recently with success in reducing biases and producing accurate error bars on physical parameters (Leja et al. 2019; Iyer et al. 2019). However, a parametric SFH model is used for this project because it confines the parameter space to a reasonable number of dimensions. Some of the shortcomings of choosing a single SFH model for such a wide variety of galaxies is discussed in Section 5.1.

In addition to the radial analysis of these galaxies, a similar SED-fitting process was done on individual star forming complexes in the galaxies. These sources were found using SExtractor Bertin & Arnouts (1996) in order to automate the process. For this analysis the images were smoothed to a common PSF and the NUV image was used as the basis for finding sources. The average size of these automatically identified sources was 14.3" and there were approximately 200 sources per galaxy on average. The distribution of physical sizes (in parsecs) of the sources changed depending on the galaxy because the minimum resolvable source depends on the distance to that galaxy. For the closest galaxy, UGC 07577, the smallest regions detectable can be  $\sim 30$  pc in radius. NGC 3938 is the furthest away at 17.90 Mpc, making the smallest sources possible  $\sim 300$  pc in radius. A maximum size of 1.5 kpc was allowed, so sources larger than this were split up into smaller regions. A recent study of the NGC 7793 found UV clumps sized 12-70 pc (Mondal et al. 2021). In comparison, the smallest size permitted for NGC 7793 in this project was  $\sim 40$  pc. The fluxes of the UV-selected sources were measured at each available wavelength and were fit to SEDs to recover their physical properties. Although the parameter space for the radial analysis allowed for the recent onset of star formation to be as old as 4 Gyr, the UV-selection of these individual star-forming complexes gives a younger upper limit for the age of these sources. Because of this,

the parameter space was changed such that  $t_{ySP}$  could be no older than 1 Gyr. Limiting the oldest  $t_{ySP}$  allowed for a finer spacing of younger values to be explored in the models.

To describe the way star formation manifests in a galaxy based on this small-scale analysis, we wanted to look at the characteristic separation between sources of similar star formation properties. The *scikit-learn* Python package (Pedregosa et al. 2011) contains numerous clustering algorithms that would be applicable to finding groups of stellar complexes with similar star formation parameters. The *k*-means clustering algorithm, where *k* is the number of groupings permitted, was chosen for this particular project. The optimal *k* for each galaxy was chosen after reviewing three classic diagnostics: the elbow method, the silhouette method, and using the approximation  $k \approx \sqrt{n/2}$  (Kodinariya & Makwana 2013). The relevant features were chosen to be three SFH parameters from the SED-fitting results ( $f_{burst}$ ,  $age_{burst}$ , and  $\tau_{burst}$ ) as well as the NUV magnitude of the UV-selected sources. Membership to each group depends on an individual source's proximity to all of the groups in the feature space, not the physical proximity to other sources in the galaxy. After the group membership of the stellar complexes were determined, the average Euclidean distance between sources within an assigned group was calculated and then normalized by the measured  $R_{25}$  for easier comparison between galaxies.

## 4 RESULTS

### 4.1 Surface Brightness and Color Profiles

The ellipse properties from the IRAF-based method for deriving  $R_{25}$  are shown in Table 4. The surface brightness profile, B-R color gradient, log specific star formation rate (sSFR) and log equivalent width (EW) profiles are given for each galaxy next to the cumulative star formation histories in Appendix A. An example of the results are shown for NGC 4242 in Figures 3 and 4. The EW( $H\alpha$ ) has often been used as an indicator for the current normalized SFR compared to the past average SFR rate (Kennicutt & Kent 1983). The EW( $H\alpha$ ) profiles are used in a limited capacity for the aforementioned issues with different  $H\alpha$  sources. However, the profiles can be looked at in a relative sense to get a better understanding of where the most star formation is occurring in a galaxy.

To calculate the sSFR profile for these galaxies, broadband indicators for SFR (FUV+24  $\mu$ m flux) and stellar mass (3.6  $\mu$ m flux) were used. The FUV+24  $\mu$ m SFR indicator was used to ensure re-radiation of the ultraviolet star formation tracer was taken into account (Hao et al. 2011). When the FUV data were unavailable, the NUV data were substituted instead as the SFR indicator and the appropriate NUV coefficient was used in the conversion. However, this was only the case for NGC 3938. As more galaxies are added to this study, more galaxies may require this slightly alternative method of deriving SFR. The mass of the stellar disc was calculated from the 3.6  $\mu$ m data, assuming a mass-to-light ratio of  $\Upsilon_{*}^{3.6\mu m} = 0.5 \pm 0.1$  (Cook et al. 2014; Meidt et al. 2014). The log(sSFR) panels show an inverse relationship with the (B-R) color gradients, as expected with the understanding that bluer populations are more actively forming stars than redder regions.

### 4.2 Global Properties

Comparing two values for each galaxy's total stellar mass, calculated through both the SED fitting of the measured integrated magnitudes



**Table 3.** Module and parameter values used for SED fitting.

Module	Parameter	Value
sfh2exp	tau_main	0.2, 0.5, 1, 5, 10 Gyr
	tau_burst	0.05, 0.1, 0.2, 1, 2 Gyr
	f_burst	0.005, 0.01, 0.05, 0.1, 0.2, 0.5, 0.75
	age	10 Gyr
	age_burst	0.01, 0.1, 0.5, 1.0, 2.0, 3.0, 4.0 Gyr
bc03	imf	Salpeter
	metallicity	0.008, 0.02, 0.05
nebular	logU	-3.0, -2.0
dustatt_modified_starburst	E_BV_lines	0.0, 0.025, 0.05, 0.1, 0.15, 0.2, 0.25, 0.3, 0.4 mag
	powerlaw_slope	-0.5, -0.4, -0.3, -0.2, -0.1, 0.0
dale2014	fracAGN	0
	alpha	0.5, 1.0, 1.25, 1.50, 1.75, 2.0, 2.25, 2.50, 3.00

**Table 4.** Ellipse properties. The centre of each ellipse may not correspond to the canonical centre of each galaxy, but is derived from the centre of the ellipse at  $R_{25}$ . Position angle (PA) is measured East of North.

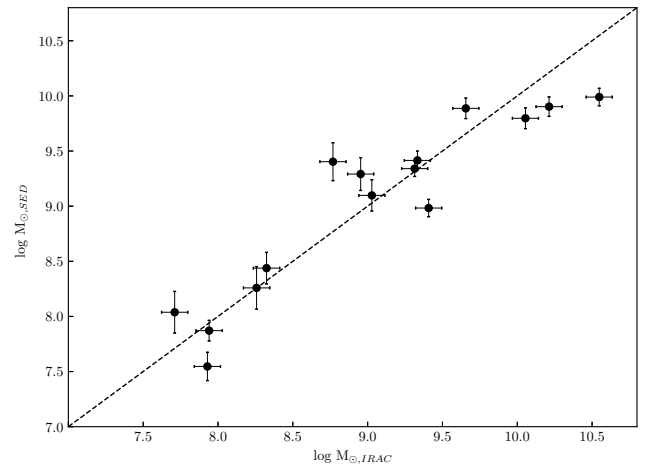
Galaxy	RA	Dec	$R_{25}$ (")	$r_e$ (")	b/a	PA (deg)
NGC 0024	00:09:56.65	-24:57:44.1	114.7	55.20	0.256	44.52
NGC 3344	10:43:31.14	24:55:20.40	206.9	59.00	0.970	-40.79
NGC 3486	11:00:23.88	28:58:32.23	178.3	77.58	0.792	82.69
NGC 3938	11:52:49.65	44:07:14.86	154.5	48.60	0.930	10.0
NGC 4068	12:04:02.48	52:35:29.50	73.47	51.30	0.602	30.49
NGC 4096	12:06:00.10	47:28:28.47	155.3	69.00	0.267	18.8
NGC 4214	12:15:39.07	36:19:44.15	206.9	61.30	0.967	-172.2
NGC 4242	12:17:29.96	45:37:07.64	137.0	84.60	0.695	30.7
NGC 4618	12:41:32.95	41:08:41.92	117.1	51.95	0.832	22.71
NGC 4625	12:41:52.52	41:16:19.12	49.34	22.35	0.913	-60.38
NGC 7793	23:57:49.52	-32:35:28.2	283.7	122.6	0.595	-80.88
UGC 07408	12:21:15.32	45:48:51.93	53.03	45.45	0.627	-83.45
UGC 07577	12:27:42.48	43:29:32.75	85.25	68.15	0.699	56.73
UGC 07608	12:28:44.95	43:13:29.93	46.53	54.30	0.497	-50.89
UGC 08320	13:14:26.56	45:55:30.60	80.54	80.75	0.424	-28.88

and by using the M/L ratio at  $3.6\mu\text{m}$ , was used as a first pass at determining whether the SED fitting process was producing reasonable results. Although the focus of this project is on the trends at radial and local scales, the results from the globally measured properties are given here. Figure 1 displays the global SED-estimated  $\log M_*$  compared to the  $\log M_*$  derived from the  $3.6\mu\text{m}$  data for the sample. Although several galaxies fall on the one-to-one correspondence, some galaxies deviate a significant amount. A possible systematic affecting the higher mass galaxies may be the contamination of PAH emission in the  $3.6\mu\text{m}$  measurements, leading to an overestimation in  $\log M_{*,\text{IRAC}}$  (Meidt et al. 2012). A more formal statistical analysis of the differences in these global measurements should be done when more of the EDGES sample is covered in future papers.

The general agreement between the two values suggests that the parameter space used here is probing the relevant values to estimate the physical properties for this sample of galaxies.

### 4.3 Radial Trends

The parameters outlined in Section 3 and Table 3 create a grid of  $\sim 4$  million models. The best-fitting models are found by computing  $\chi^2$  from the residuals and photometric uncertainty, and then the

**Figure 1.** Comparison of the total stellar mass estimates from SED fitting and from  $3.6\mu\text{m}$ -to-mass conversion (Hao et al. 2011). The dashed line shows a one-to-one correspondence.

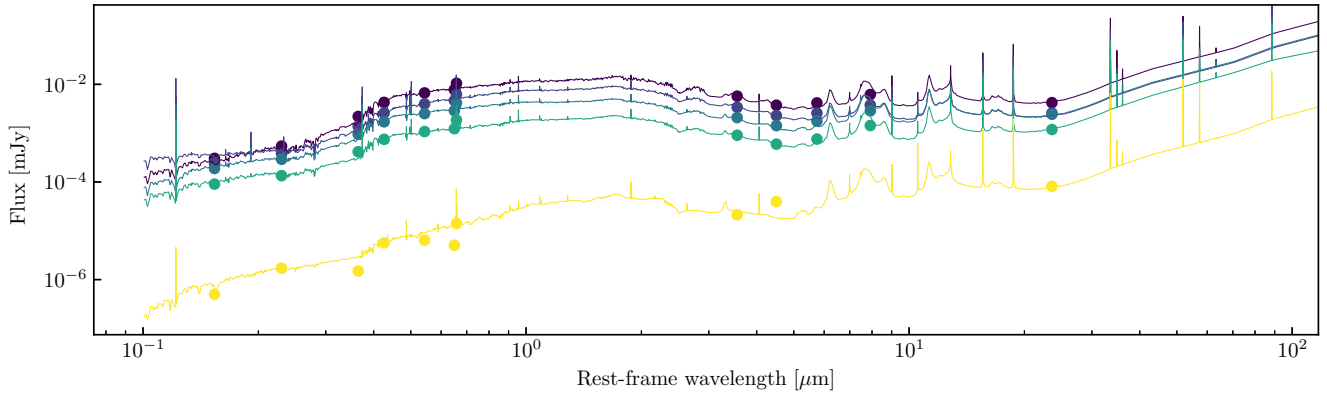


**Figure 2.** The best-fitting SEDs for five of the annuli covering NGC 4242. The innermost annulus is the brightest, with each consecutive annulus getting dimmer. In the final annulus (yellow line), the IRAC 3 & 4 filters did not have signal, so they were left out of the fitting.

likelihood-weighted parameters are recorded. The full statistical process of finding the output parameters for the SED fitting process are outlined in Boquien et al. (2019). The best-fit SED for each annulus in NGC 4242, along with the observed fluxes, are shown in Figure 2. Cumulative star formation histories were constructed from the Bayesian-estimated SFH parameters for each annulus of each galaxy. Figure 3 shows the five annuli that cover the extent of NGC 4242’s disc, including information on the B-R color and the form of the cumulative SFH for each annulus. The line thickness depends on the annulus’ distance from the galaxy’s photometrically-determined centre, such that thicker lines are closer to the centre. As mentioned in Section 3, each galaxy was evaluated individually to determine how many annuli would be appropriate to fully explore the farthest extents of each galaxy. In the case of NGC 4242, five concentric ellipses were used to capture the relevant parts of the galaxy, with all five annuli having their goodness of fit below the set threshold of reduced  $\chi^2$ ,  $\chi^2_{\nu} = 15$ . In the majority of cases where a region’s SED had a reduced  $\chi^2$  above the threshold, the annulus was on a low surface brightness part of the galaxy, away from the often bright nucleus.

Figure 3 matches the expected trends in SF, based on the photometric measurements seen in the two middle panels of Figure 4. Between the centre and farthest reaches of this galaxy, there is a region of elevated star formation. The innermost and outermost regions of the galaxy underwent bursts at earlier times ( $\sim 1$ – $2$  Gyr ago) than the middle region, which experienced elevated star formation starting 500 Myr ago. The (B-R) coloring of each region is not corrected for internal extinction, so the correlation between bluer colors and more recent star formation cannot be immediately drawn without exploring the dust attenuation. The SED-derived dust parameters (such as shape of the attenuation curve) have been shown to be the least accurate parameters returned in the fitting process (Giovannoli et al. 2011; Boquien et al. 2012), so the dust results are mentioned here only briefly. In most cases, the attenuation ( $A_V$ ) showed smooth transitions as a function of radius, suggesting there were not many instances where degeneracies brought a chaotic nature to the results, or affected other SED-derived parameters.

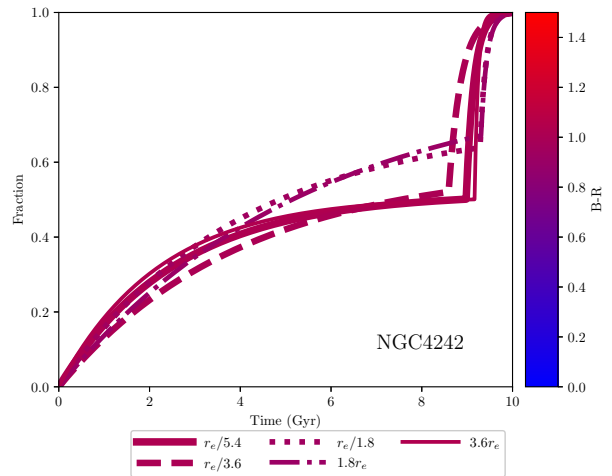


**Figure 3.** Cumulative SFH for the five well-fit annuli of NGC 4242. The stellar mass fraction is equal to one at current times. As stated in Section 3, the older population is set to start forming 10 Gyr ago, while the younger population has a flexible start time,  $t_{y,SP}$ . With this framework, the x-axis shows time since the oldest stars were allowed to form.

#### 4.4 Stellar Complexes

Looking at star formation on a local scale helps alleviate some of the shortcomings of the radial analysis. The azimuthal averaging needed to create surface brightness profiles smoothed over many of the important structural features in these galaxies, specifically the spiral arms of the more massive galaxies. As a result, areas of recent star formation were averaged with adjacent areas of older stellar populations, biasing some results towards older SFHs than what may be truly characteristic of parts of a galaxy. In a similar vein, dwarf irregulars undergoing clumpy star formation may not be the ideal candidates for the radial treatment. The stellar complex analysis presented here is a morphology-independent way to look at the most recent areas of star formation in a wide range of galaxies.

The SED-fitting results of the UV-selected sources were used to examine the way different stellar populations exist in a galaxy. Are younger populations often grouped together or more spread throughout the disc? In the  $\Lambda$ CDM framework, it should be expected to find

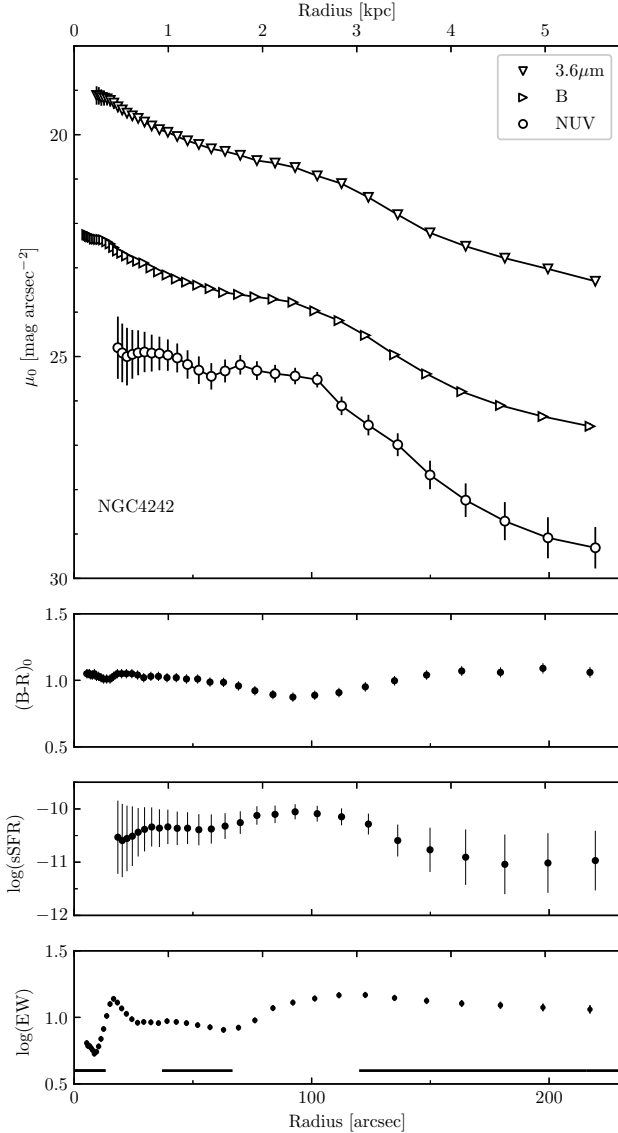


**Figure 4.** The results from the photometric measurements of NGC 4242. The innermost annulus size is set by the resolution of the data. The variations in the colour gradient are mirrored in the  $\log(\text{sSFR})$  profile, showing a connection between B-R colour and SFR. The bluest region in NGC 4242 is coincident with the highest sSFR and EW( $\text{H}\alpha$ ) values. All of these radial profiles are measured from the images using finely-spaced, azimuthally-averaged annuli. In the bottom panel, solid horizontal lines are used to show the larger radial bins used for SED fitting.

older populations more clumped together (often near the centre of the galaxy) than the areas of recent/current star formation. As an initial test of this concept, the scatter within groups of similar SFH properties was measured. Figure 5 shows the results of the clustered sources from all of the galaxies. The older (but still relatively young) groups of star formation were found to be closer together (lower average separation) than the groups of extremely recent onsets of star formation, as expected.

Although there may be an inverse relationship between the average separation between star-forming sources within a group of similar SFHs and the  $t_{\text{ySFR}}$  of that group’s common SFH, the results seen in

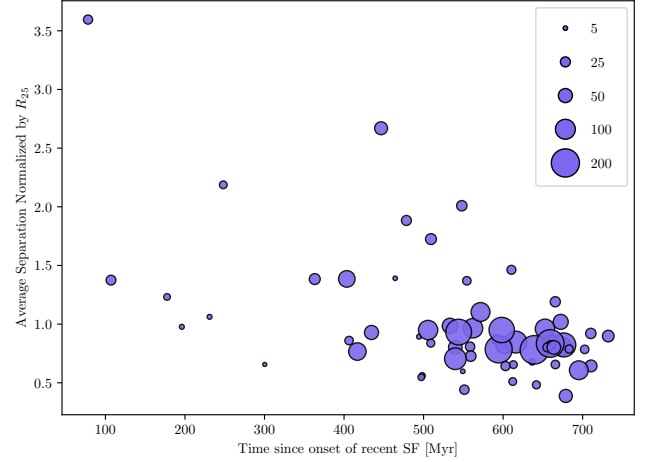


**Figure 5.** The average physical separation between stellar complexes within a group assigned by the k-means algorithm versus the average time since the last onset of star formation ( $\text{age}_{\text{burst}}$ ). The size of each point is determined by the number of stellar complexes in each group. The smallest point has only four sources (a cluster in NGC 4242) and the largest has 205 sources (a cluster in NGC 7793). Because the sources were UV-selected, the lack of older clusters is expected. The uncertainty on the time of the burst is large, with an average of 200 Myrs.

Figure 5 may be influenced by other things. Although the distances between sources within a common cluster were normalized by the size of the galaxy they are contained within so that the results could be compared between galaxies without biasing results, other biases arise. For example, the clusters with the seven highest values of average separation ( $> 1.4R_{25}$  in separation) come from just two galaxies, NGC 4625 and UGC 07608. NGC 4625 has an extended XUV disc with UV emission extending out to  $4\times$  its optical radius (Gil de Paz et al. 2005); therefore, normalizing the separation to  $R_{25}$  biases the normalized, average separation to higher values than the rest of the galaxies that do not have the extended UV emission. In a similar vein, UGC 7608 is a low surface brightness galaxy where  $R_{25}$  encompasses less of the total emission of the galaxy. This led to more UV sources being well-beyond  $R_{25}$  and, therefore, led to more clustered sources appearing to have higher average separation in Figure 5.

Another hidden variable in this stellar complex analysis is that it lacks information on the intrinsic nature of these sources. Their sizes are not encoded into these results, but may contain information regarding the more detailed stage of star formation these regions are experiencing. Hierarchical star formation on scales similar to those discussed here have been studied extensively (e.g., Efremov 1995; Elmegreen & Efremov 1996; Elmegreen & Salzer 1999). Although the detailed analysis of the scale and nature of the UV-selected sources are beyond the scope of this paper, the information is available to be studied in a future project. Adding more galaxies to this sample may provide the information needed to draw more quantitative conclusions about the distribution of young star forming regions in local star forming galaxies.

## 5 DISCUSSION

### 5.1 Comparing to Resolved Stellar Populations

Some of the galaxies in this sample are close enough to have *HST* resolved photometry, making it possible to use CMDs to recover detailed SFHs. In particular, [McQuinn et al. \(2010\)](#) studied NGC 4068 and NGC 4214, exploring their recent/current starbursting characteristics. Their SFH's based strictly on stellar evolutionary models suggest that the most recent burst in NGC 4068 started at about 500 Myr, with which the three inner regions of our radial analysis agree (Figure A14). The SFH from the resolved stellar population of NGC 4214 ([McQuinn et al. 2010](#)) suggests that there were elevations in SFR 1-2 Gyr and <500 Myr ago (see their Figures 8 & 9). The results of our radial analysis show that different radial components of the galaxy may have experienced these two episodes of elevated SF. The inner regions have more recent star formation, while the outer regions increasingly see older  $t_{ySP}$ . In these ways, the radial analysis of SED-derived SFHs agree with past studies of resolved stellar populations in these two galaxies.

The results of the individual stellar complex SED-fitting for NGC 4068 (and NGC 4214) are shown in Figure 6. The luminosity-weighted, normalized histograms of the  $t_{ySP}$  values for NGC 4068 and NGC 4214 can be compared to the recent SFHs of [McQuinn et al. \(2010\)](#). The CMD-derived SFHs are expected to have more resolution and less uncertainty than the currently presented method, but the general trends should be comparable. The common value of  $t_{ySP} \approx 500$  Myr among many of the UV-selected sources in NGC 4068 align with the idea that NGC 4068 began a large onset of star formation at about that time. There are not many star-forming complexes with  $t_{ySP} < 500$  Myr for NGC 4068. This result combined with the  $H\alpha$  equivalent width profile with consistently high values (provided in Figure A13), suggests that the elevated levels of star formation that began  $\sim 500$  Myr years ago has persisted at a consistent level from then until present times. These conclusions agree with the results of the CMD-derived SFH for NGC 4068 in [McQuinn et al. \(2010\)](#).

On the other hand, NGC 4214's individual sources appear to have a more bimodal distribution of  $t_{ySP}$  (Figure 6). While this shape is similar to the CMD-derived SFH presented in [McQuinn et al. \(2010\)](#), the peaks (450 & 175 Myr for [McQuinn et al. \(2010\)](#) and 600 & 200 Myr for this project) do not directly align. This difference in times could be due to either binning or SED-based uncertainty issues. With more testing and validation, extending this individual UV source analysis to galaxies more distant than  $\sim 8$  Mpc may allow for SFHs to be studied on smaller scales when resolved stellar populations are harder to observe. Presenting the SED-derived SFHs in this way may also alleviate some of the difficulties associated with having to choose between strictly parametric forms of SFHs, since the distribution of SED results across a galaxy may be more insightful than using single  $\tau$  value for the entire galaxy.

Another galaxy from our sample that has had its CMD-derived SFH computed was NGC 7793 in [Radburn-Smith et al. \(2012\)](#) and [Sacchi et al. \(2019\)](#). Both of their results suggest that about 80% of the galaxy's stars were formed within the last 8 Gyr and 40% within the last 4 Gyr. Our results (Figure A29) agree with their cumulative SFH's, although the shapes from our analysis are different. As mentioned before, a single parametric SFH (the double exponential form) was used for the entire sample, so it is expected that some galaxies are more well-fit than others. In the case of NGC 7793, a delayed SFH might be the more appropriate functional form to have chosen, but the flexibility of the available parameters produced results that appear quite similar to the single parameter  $\tau$  models in the case of NGC 7793.

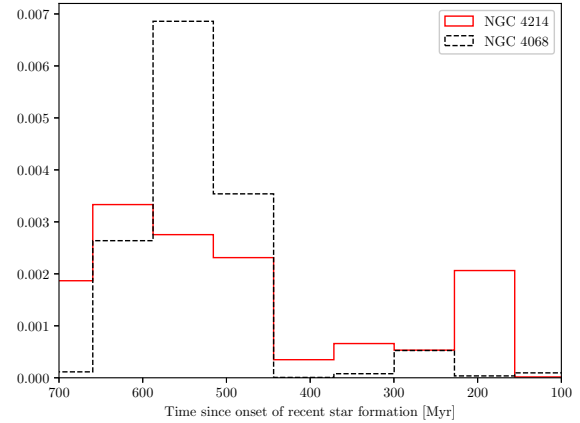


**Figure 6.** Normalized histogram of the SED-derived burst age for the UV-selected stellar complexes. In order to account for the differences in other properties, like size of the source and the strength of the current SFR, the times are weighted by the total luminosity of the source. Comparing these results to those in [McQuinn et al. \(2010\)](#), our results show increased onsets of SF at the most recent times ( $< 1$  Gyr).

### 5.2 Stellar Migration

Numerical simulations such as those in [Radburn-Smith et al. \(2012\)](#) have been utilized to explain the breaks in surface brightness profiles via radial migration. In the case of [Radburn-Smith et al. \(2012\)](#), NGC 7793, one of the galaxies in this sample, showed evidence that the outer region of the galaxy was older than the interior because of strong radial stellar migration. Type I and III surface brightness profiles (those with pure exponential profiles and those with upbending profiles after the break radius) are linked with high radial migration efficiency ([Ruiz-Lara et al. 2017](#)) and are not uncommon, so these dynamical effects should not be ignored in the context of stellar populations. The deep 3.6 and 4.5  $\mu\text{m}$  images from EDGES can help determine which galaxies in our sample may be exhibiting the observational evidence of stellar migration from their surface brightness profiles ([Staudaher et al. 2019](#)). If stellar migration is a major factor in these galaxies, our initial assumption that the concentric ellipses defined from the photometry evolve independently of each other may falter. In this case, it would be important to create a system in which the SED-fitting process would have knowledge of neighboring annuli as it fits each annulus.

## 6 CONCLUSION

We have presented new UBVR observations from the WIYN 0.9m telescope for several nearby galaxies. These observations combined with archival *GALEX* and *Spitzer* imaging allow us to take a deeper look into the radial trends of galaxies in the local volume. Surface brightness profiles were presented for each galaxy, based on fixed-ellipse photometry. Classic star formation rate tracers, UV + mid-IR and  $H\alpha$  fluxes, were examined as a function of radius to explore regions of recent star formation, on two different time-scales (100 and 10 Myrs respectively). In conjunction with these classic star formation indicators, SED fitting was utilized to derive more star formation properties, with a focus on star formation histories. While there is a plethora of parameters that SED fitting can infer, this



analysis focused on the most recent onset of star formation ( $t_{y,SP}$ ) in a double-exponential SFH model.

Radial SFHs often showed the same trends seen in the photometric profiles, with small incremental changes in star formation of adjacent ellipses. Larger changes in the SED-inferred SFHs between radial bins often signified a turnover from one structural feature to another (the difference between an old bulge and a younger stellar disc, for example). For the spiral galaxies in this sample, the intermediate regions showed the youngest stellar populations which suggests a growing stellar disc within a larger, older stellar halo, agreeing with the results of D'Souza et al. (2014) and Dale et al. (2016).

The UV-selected stellar complex analysis provided local insight - more than was possible with the azimuthally-averaged radial analysis - about the regions of youngest star formation in each galaxy. We showed a tentative relationship between the ages of clusters of UV-sources and the way they are distributed throughout a galaxy. Stellar complexes that have not recently begun star formation are more likely to be clustered together. Future studies similar to this may provide direct constraints on this relationship. There was no discernible difference in this relationship when morphologies were taken into consideration. This conclusion was counterintuitive due to the differences in color and SFH gradients seen in the radial analysis of the same galaxies.

In the future, we hope to utilize the methods presented here on a larger sample of nearby galaxies to better understand the variety of stellar population distributions possible in a  $\Lambda$ CDM universe. With a larger sample comes the possibility of placing better physical constraints on possible star formation properties on different scales (global, radial, or local). These constraints can better inform the realistic simulations of galaxy evolution.

## ACKNOWLEDGEMENTS

The authors thank the referee for taking the time to provide thoughtful feedback on this paper. The authors would also like to thank the CIGALE team for making their SED-fitting software publically available. This project is funded by NASA award NNX17AF17G. MVS worked on this project as a recipient of the Indiana Space Grant Consortium Doctoral Fellowship. This research made use of Astropy,<sup>2</sup> a community-developed core Python package for Astronomy (Astropy Collaboration et al. 2018). This research has made use of the NASA/IPAC Extragalactic Database, which is funded by the National Aeronautics and Space Administration and operated by the California Institute of Technology.

## DATA AVAILABILITY

The GALEX and Spitzer data underlying this article were accessed from public sources. The derived data generated in this research will be shared on reasonable request to the corresponding author.

## REFERENCES

- Abadi M. G., Navarro J. F., Steinmetz M., Eke V. R., 2003, *ApJ*, **597**, 21  
 Alberts S., et al., 2011, *ApJ*, **731**, 28  
 Anders P., Fritze-v. Alvensleben U., 2003, *A&A*, **401**, 1063  
 Annunzi A., et al., 2020, *MNRAS*, **497**, 229

- Astropy Collaboration et al., 2018, *AJ*, **156**, 123  
 Aumer M., White S. D. M., Naab T., Scannapieco C., 2013, *MNRAS*, **434**, 3142  
 Bagetakos I., Brinks E., Walter F., de Blok W. J. G., Usero A., Leroy A. K., Rich J. W., Kennicutt R. C. J., 2011, *AJ*, **141**, 23  
 Bakos J., Trujillo I., Pohlen M., 2008, *ApJ*, **683**, L103  
 Barnes J. E., Hernquist L., 1992, *Nature*, **360**, 715  
 Barnes K. L., van Zee L., Dale D. A., Staudaher S., Bullock J. S., Calzetti D., Chandar R., Dalcanton J. J., 2014, *ApJ*, **789**, 126  
 Bertin E., Arnouts S., 1996, *A&AS*, **117**, 393  
 Bertola F., 1967, *Mem. Soc. Astron. Italiana*, **38**, 417  
 Boissier S., Prantzos N., 1999, *MNRAS*, **307**, 857  
 Boissier S., Prantzos N., 2000, *MNRAS*, **312**, 398  
 Boquien M., et al., 2012, *A&A*, **539**, A145  
 Boquien M., Burgarella D., Roehlly Y., Buat V., Ciesla L., Corre D., Inoue A. K., Salas H., 2019, *A&A*, **622**, A103  
 Bremnes T., Binggeli B., Prugniel P., 1999, *A&AS*, **137**, 337  
 Broeils A. H., 1992, PhD thesis, Univ. Groningen  
 Bruzual G., Charlot S., 2003, *MNRAS*, **344**, 1000  
 Bullock J. S., Johnston K. V., 2005, *ApJ*, **635**, 931  
 Bush S. J., Wilcots E. M., 2004, *AJ*, **128**, 2789  
 Bush S. J., Kennicutt R. C., Ashby M. L. N., Johnson B. D., Bresolin F., Fazio G., 2014, *ApJ*, **793**, 65  
 Cairós L. M., Caon N., Vílchez J. M., González-Pérez J. N., Muñoz-Tuñón C., 2001, *ApJS*, **136**, 393  
 Calzetti D., Armus L., Bohlin R. C., Kinney A. L., Koornneef J., Storchi-Bergmann T., 2000, *ApJ*, **533**, 682  
 Carignan C., 1985, *ApJS*, **58**, 107  
 Chemin L., Carignan C., Drouin N., Freeman K. C., 2006, *AJ*, **132**, 2527  
 Cook D. O., et al., 2014, *MNRAS*, **445**, 899  
 Cooper A. P., D'Souza R., Kauffmann G., Wang J., Boylan-Kolchin M., Guo Q., Frenk C. S., White S. D. M., 2013, *MNRAS*, **434**, 3348  
 D'Souza R., Kauffman G., Wang J., Vegetti S., 2014, *MNRAS*, **443**, 1433  
 Dale D. A., et al., 2009, *The Astrophysical Journal*, **703**, 517  
 Dale D. A., Helou G., Magdis G. E., Armus L., Díaz-Santos T., Shi Y., 2014, *ApJ*, **784**, 83  
 Dale D. A., et al., 2016, *AJ*, **151**, 4  
 Dale D. A., et al., 2020, *AJ*, **159**, 195  
 Dicaire I., et al., 2008, *MNRAS*, **385**, 553  
 Efremov Y. N., 1995, *AJ*, **110**, 2757  
 El-Badry K., Wetzel A., Geha M., Hopkins P. F., Kereš D., Chan T. K., Faucher-Giguère C.-A., 2016, *ApJ*, **820**, 131  
 Elmegreen B. G., Efremov Y. N., 1996, *ApJ*, **466**, 802  
 Elmegreen D. M., Elmegreen B. G., 1984, *ApJS*, **54**, 127  
 Elmegreen B. G., Hunter D. A., 2006, *ApJ*, **636**, 712  
 Elmegreen D. M., Salzer J. J., 1999, *AJ*, **117**, 764  
 Eskridge P. B., et al., 2002, *ApJS*, **143**, 73  
 Fazio G. G., et al., 2004, *ApJS*, **154**, 10  
 Fitzpatrick E. L., 1999, *PASP*, **111**, 63  
 Gallagher J. S. I., Hunter D. A., 1986, *AJ*, **92**, 557  
 García-Ruiz I., Sancisi R., Kuijken K., 2002, *A&A*, **394**, 769  
 Ghosh S., Jog C. J., 2018, *New Astron.*, **63**, 38  
 Gil de Paz A., et al., 2005, *ApJ*, **627**, L29  
 Giovannoli E., Buat V., Noll S., Burgarella D., Magnelli B., 2011, *A&A*, **525**, A150  
 Hao C.-N., Kennicutt R. C., Johnson B. D., Calzetti D., Dale D. A., Moustakas J., 2011, *ApJ*, **741**, 124  
 Ho L. C., Filippenko A. V., Sargent W. L. W., 1997, *ApJS*, **112**, 315  
 Holwerda B. W., Pirzkal N., Heiner J. S., 2012, *MNRAS*, **427**, 3159  
 Huchra J. P., Geller M. J., Gallagher J., Hunter D., Hartmann L., Fabbiano G., Aaronson M., 1983, *ApJ*, **274**, 125  
 Hunt L. K., et al., 2019, *A&A*, **621**, A51  
 Hunter D. A., Elmegreen B. G., 2006, *ApJS*, **162**, 49  
 Hunter D. A., Wilcots E. M., van Woerden H., Gallagher J. S., Kohle S., 1998, *ApJ*, **495**, L47  
 Hunter D. A., Hunsberger S. D., Royce E. W., 2000, *ApJ*, **542**, 137  
 Iyer K. G., Gawiser E., Faber S. M., Ferguson H. C., Koekemoer A. M., Pacifici C., Somerville R., 2019, arXiv e-prints, p. [arXiv:1901.02877](https://arxiv.org/abs/1901.02877)

<sup>2</sup> <http://www.astropy.org>

- Jacobs B. A., Rizzi L., Tully R. B., Shaya E. J., Makarov D. I., Makarova L., 2009, *AJ*, **138**, 332
- Kaczmarek J. F., Wilcots E. M., 2012, *AJ*, **144**, 67
- Karachentsev I. D., et al., 2003, *A&A*, **398**, 467
- Kennicutt R. C., Evans N. J., 2012, *ARA&A*, **50**, 531
- Kennicutt R. C. J., Kent S. M., 1983, *AJ*, **88**, 1094
- Kennicutt Robert C. J., et al., 2003, *PASP*, **115**, 928
- Kodinariya T. M., Makwana P. R., 2013, *International Journal*, **1**, 90
- Larson R. B., Tinsley B. M., 1978, *ApJ*, **219**, 46
- Leitherer C., Li I. H., Calzetti D., Heckman T. M., 2002, *ApJS*, **140**, 303
- Leja J., Carnall A. C., Johnson B. D., Conroy C., Speagle J. S., 2019, *ApJ*, **876**, 3
- MacArthur L. A., Courteau S., Bell E., Holtzman J. A., 2004, *ApJS*, **152**, 175
- McQuinn K. B. W., et al., 2010, *ApJ*, **721**, 297
- McQuinn K. B. W., Skillman E. D., Dolphin A. E., Berg D., Kennicutt R., 2017, *AJ*, **154**, 51
- Meidt S. E., et al., 2012, *ApJ*, **744**, 17
- Meidt S. E., et al., 2014, *ApJ*, **788**, 144
- Mentuch Cooper E., et al., 2012, *ApJ*, **755**, 165
- Monachesi A., et al., 2013, *ApJ*, **766**, 106
- Mondal C., Subramaniam A., George K., Postma J. E., Subramanian S., Barway S., 2021, arXiv e-prints, p. arXiv:2101.11314
- Muñoz-Mateos J. C., et al., 2009, *ApJ*, **703**, 1569
- Muñoz-Mateos J. C., Boissier S., Gil de Paz A., Zamorano J., Kennicutt R. C. J., Moustakas J., Prantzos N., Gallego J., 2011, *ApJ*, **731**, 10
- Noeske K. G., et al., 2007, *ApJ*, **660**, L43
- Noll S., Burgarella D., Giovannoli E., Buat V., Marcellac D., Muñoz-Mateos J. C., 2009, *A&A*, **507**, 1793
- Patra N. N., Jog C. J., 2019, *MNRAS*, **488**, 4942
- Patterson R. J., Thuan T. X., 1996, *ApJS*, **107**, 103
- Pedregosa F., et al., 2011, *Journal of Machine Learning Research*, **12**, 2825
- Poznanski D., et al., 2009, *ApJ*, **694**, 1067
- Prugniel P., Heraudeau P., 1998, *A&AS*, **128**, 299
- Radburn-Smith D. J., et al., 2012, *ApJ*, **753**, 138
- Reddy N. A., Pettini M., Steidel C. C., Shapley A. E., Erb D. K., Law D. R., 2012, *ApJ*, **754**, 25
- Richards E. E., et al., 2016, *MNRAS*, **460**, 689
- Richards E. E., et al., 2018, *MNRAS*, **476**, 5127
- Rossa J., Dettmar R. J., 2003, *A&A*, **406**, 505
- Ruiz-Lara T., et al., 2017, *A&A*, **604**, A4
- Sacchi E., et al., 2019, *ApJ*, **878**, 1
- Salim S., et al., 2016, *ApJS*, **227**, 2
- Salpeter E. E., 1955, *ApJ*, **121**, 161
- Sargent W. L. W., Filippenko A. V., 1991, *AJ*, **102**, 107
- Schlafly E. F., Finkbeiner D. P., 2011, *ApJ*, **737**, 103
- Sellwood J. A., Binney J. J., 2002, *MNRAS*, **336**, 785
- Sorce J. G., Tully R. B., Courtois H. M., Jarrett T. H., Neill J. D., Shaya E. J., 2014, *MNRAS*, **444**, 527
- Staudaher S. M., Dale D. A., van Zee L., 2019, *MNRAS*, **486**, 1995
- Swaters R. A., 1999, PhD thesis, -
- Swaters R. A., van Albada T. S., van der Hulst J. M., Sancisi R., 2002, *A&A*, **390**, 829
- Thilker D. A., et al., 2005, *ApJ*, **619**, L79
- Thilker D. A., et al., 2007, *ApJS*, **173**, 538
- Tully R. B., Fisher J. R., 1988, *Catalog of Nearby Galaxies*
- Tully R. B., et al., 2013, *AJ*, **146**, 86
- Tully R. B., Courtois H. M., Sorce J. G., 2016, *AJ*, **152**, 50
- Verdes-Montenegro L., Bosma A., Athanassoula E., 2000, *A&A*, **356**, 827
- Walter F., Brinks E., de Blok W. J. G., Bigiel F., Kennicutt Robert C. J., Thornley M. D., Leroy A., 2008, *AJ*, **136**, 2563
- Weisz D. R., et al., 2011, *ApJ*, **739**, 5
- Williams B. F., Dalcanton J. J., Gilbert K. M., Seth A. C., Weisz D. R., Skillman E. D., Dolphin A. E., 2011, *ApJ*, **735**, 22
- Zgirski B., et al., 2017, *ApJ*, **847**, 88
- Zhang H.-X., Hunter D. A., Elmegreen B. G., Gao Y., Schruha A., 2012, *AJ*, **143**, 47
- de Blok W. J. G., Walter F., Brinks E., Trachternach C., Oh S. H., Kennicutt R. C. J., 2008, *AJ*, **136**, 2648
- de Jong R. S., 1996, *A&A*, **313**, 377
- de Vaucouleurs G. H., de Vaucouleurs A., Shapley H., 1964, *Reference catalogue of bright galaxies*
- van Eymeren J., Jütte E., Jog C. J., Stein Y., Dettmar R. J., 2011, *A&A*, **530**, A29
- van Zee L., Haynes M. P., Salzer J. J., Broeils A. H., 1997, *AJ*, **113**, 1618
- van Zee L., Dale D. A., Barnes K. L., Staudaher S., Calzetti D., Dalcanton J. J., Bullock J. S., Chandar R., 2012, in *American Astronomical Society Meeting Abstracts* #220. p. 433.08
- van der Hulst J. M., van Albada T. S., Sancisi R., 2001, in *Hibbard J. E., Rupen M., van Gorkom J. H., eds, Astronomical Society of the Pacific Conference Series Vol. 240, Gas and Galaxy Evolution*. p. 451
- van der Kruit P. C., Shostak G. S., 1982, *A&A*, **105**, 351

## APPENDIX A: PHOTOMETRIC MEASUREMENTS & HI OBSERVATIONS

For the 14 galaxies not shown in the body of this paper (see Figures 3 and 4 for NGC 4242), the photometric measurements and radial cumulative star formation histories are described here. As described in Section 4.1, the surface brightness profiles of each galaxy at three wavelengths (NUV, B, and IRAC Channel 1) are measured. The (B-R) color gradient is shown because a change in optical colors can be linked to a change in stellar populations (Larson & Tinsley 1978). The sSFR profile, from the FUV+24 $\mu$  SFR indicator (Hao et al. 2011), and the H $\alpha$  EW profile trace the recent star formation on different time scales (100 Myr and 10 Myr time-scales respectively)

This appendix also presents the HI measurements and color images of the galaxies in the sample. The HI data comes from a variety of sources, shown in Table A1. The HI data is presented as additional observations that can be drawn from to form conclusions about the past, present, and future ability of a galaxy to form stars and grow its stellar disc. The top left panel shows the IRAC 3.6 $\mu$ m image from EDGES, with an HI surface density contour superimposed. Unless stated otherwise, the contour represents  $1 \times 10^{20}$  atoms cm $^{-2}$ . The top left panel shows an RGB color image where red is 3.6 $\mu$ m from Spitzer, green is R from WIYN 0.9m, and blue is B + FUV from WIYN 0.9m/GALEX, unless noted otherwise. Although the surface brightness profile analysis and SED fitting relied on the azimuthal averaging of concentric radial bins, there are often features that can be lost in this averaging process. The color images are designed to bring attention to some of the features that may be important in further understanding the growth of the stellar disc. The bottom left image is the HI surface density contours starting at  $0.5 \times 10^{20}$  atoms cm $^{-2}$ . The bottom right image is the velocity field, including some annotations to indicate the contour step sizes. In all panels that include HI data, the beam size is represented in the bottom left corner.

**Table A1.** Published HI data references: (1) van der Hulst et al. (2001); (2) Richards et al. (2016); (3) Richards et al. (2018); (4) Walter et al. (2008); (5) Swaters et al. (2002); (6) AW618 C config.: Bush & Wilcots (2004), AW618 B,C config.: Kaczmarek & Wilcots (2012); (7) Hunter et al. (1998); (8) Patterson & Thuan (1996); (9) Broeils (1992). \* only one polarization

Galaxy	Telescope; array	Project code	Time on source (h)	Chan. sep. (km s <sup>-1</sup> )	Beam size (arcsec)	Beam PA (deg)	Noise (mJy beam <sup>-1</sup> )	Pub. ref
NGC 0024	VLA; DnC, CnB	AF219, AC343	9.5	2.6	30.0 x 21.6	11.2	1.0	–
NGC 3344	WSRT	WHISP	12	4.1	62.0 x 48.8	0.0	1.9	(1)
NGC 3486	VLA; C	13A-107	6.6	5.0	25.5 x 17.7	55.8	0.47	(2)
NGC 3938	VLA; C, D	AW358	6.0*	2.6	27.5 x 24.6	9.50	1.1	–
NGC 4068	VLA; C	16A-013	6.8	5.0	18.7 x 16.7	43.7	0.46	(3)
NGC 4096	VLA; C	16A-013	7.4	5.0	20.1 x 16.6	-75.9	0.47	(3)
NGC 4214	VLA; B, C, D	AM418	11	5.2	21.7 x 19.4	-23.7	0.65	(4)
NGC 4242	WSRT	WHISP	12	4.1	30.9 x 30.8	0.0	4.0	(5)
NGC 4618/4625	VLA; B, C, D	AW618, AO108, AO101	38	5.2	19.7 x 18.2	84.4	0.25	(6)
NGC 7793	VLA; BnA,CnB,DnC	AW605	9.5	2.6	15.6 x 10.9	10.7	0.92	(4)
UGC 07408	WSRT	WHISP	12	2.1	17.5 x 12.7	0.0	4.3	(5)
UGC 07577	VLA; D	AH540	0.7 *	5.2	60.6 x 55.5	81.2	1.5	(7)
UGC 07608	VLA	AP198	1.7	2.58	18.8 x 18.1	67.4	1.6	(8)
UGC 08320	WSRT	–	48	2.1	14.0 x 19.0	0.0	1.1	(9)

## A1 NGC 0024

NGC 0024 has only a moderate B-R gradient, and not a much variation in sSFR outside of the bulge, suggesting a fairly uniform SFH. The cumulative SFH reflects this. This galaxy's high inclination has been noted in observations of its HI and H $\alpha$  distributions (Chemin et al. 2006; Dicaire et al. 2008). As it is one of the more highly inclined galaxies in the sample, NGC 0024's lack of variation across the disc and red (B-R) values may be caused by inclination effects. The consistently elevated values of log(sSFR) and log(EW) observed in this radial analysis agrees with the even distribution of H $\alpha$  noted in Rossa & Dettmar (2003). The SED-derived SFHs show a similar consistency across the disc, even with more coarsely-spaced bins. A large fraction of star formation began across the entire galaxy approximately 2 Gyr ago.

## A2 NGC 3344

NGC 3344 has a well-established strong B-R color gradient (Prugniel & Heraudeau 1998). NGC 3344 has also been identified as having an XUV disc that fades more slowly than the optical disc (Thilker et al. 2007). The analysis of the observations done here show both of these attributes of NGC 3344. As is seen in the colour image of Figure A6, as well as the profiles of Figure A4, NGC 3344 has a very red (bright in the NIR) centre, but a strong young, blue (particularly in the B+NUV) stellar component in the outskirts of the galaxy. The SED-fitted, cumulative SFH results show a variation in time of the onset of recent star formation across the disc. A recent, strong burst of star formation seen in the annulus reaching out to  $3.6r_e$  represents a region that coincides with the highest sSFR values ( $r_e = 59''$ ).

The inner and outer rings, defined in Verdes-Montenegro et al. (2000), are most clearly seen in the HI (Figure A6). The HI data for NGC 3344 was taken from the Westerbork H I Survey of Spiral and Irregular Galaxies (WHISP) project (Swaters et al. 2002). The extended HI on the eastern side of the galaxy could be indicative of interaction. Although the evidence for interaction is axisymmetric, the extended B+UV emission (shown in blue in the RGB image) appears to show azimuthal symmetry. The bluest regions with the highest sSFR values are outside of  $R_{25}$  but are well within the HI disc, suggesting that the stellar disc is actively growing.

## A3 NGC 3486

With the exception with the outer most ring, NGC 3486 has one of the most obvious examples of  $t_{ySP}$  decreasing and  $f_{burst}$  increasing with galactocentric radius. The central region is host to a possible Type 2 Seyfert (Ho et al. 1997; Annunier et al. 2020). The outermost region, although slightly bluer than the intermediate regions, has a similar  $t_{ySP}$  as the intermediate regions. This combination of information may be a metallicity effect, caused by a small low-metallicity stellar halo.

There are two HI arcs extending from the southeast and northwest parts of NGC 3486 (Figure A9). However, these features appear to be rotating with the rest of the galaxy as expected by the velocity field contours. The wiggle seen just outside  $D_{25}$  in the velocity contours roughly coincides with the downbend seen in the  $3.6\mu\text{m}$  surface brightness profile of Figure A7. The color image shows a bright, red bulge, coinciding with a region of decreased HI surface density.

## A4 NGC 3938

NGC 3938 is a nearly face-on and symmetric Sc galaxy. This galaxy has also been observed as part of the SINGS sample and its multiwavelength surface brightness profiles have been documented (Muñoz-Mateos et al. 2009). Similar to NGC 3344, NGC 3938 has prominent B+NUV emission at its edges in the colour image of A12. The SED-fitting results in Figure A11 show that NGC 3938 does not have much radial variation in SFH. Prior analysis of neutral gas distribution and kinematics is presented in van der Kruit & Shostak (1982). The HI (Figure A12) does not extend much past the stellar disk and is rather symmetric in its velocity.

## A5 NGC 4068

NGC 4068 is a starbursting dwarf galaxy, identified by its extremely blue colors (Gallagher & Hunter 1986). SED-derived SFHs, shown in Figure A14, agree with the CMD-derived SFH of McQuinn et al. (2010). Because NGC 4068 has a moderate blue to red gradient, its SED results were expected to have a proportional relationship between  $t_{ySP}$  and radius. Even with a moderate color gradient, the

color profile shows consistently bluer (B-R) values ( $(B-R) \leq 1$  everywhere) than most other galaxies in the sample. The SED-derived results of the three innermost regions suggest that about 50% of the stars in this galaxy formed within the past 1 Gyr, where the burst of star formation has been largely located.

Figure A15 shows how the HI extends to the south much farther than the stellar disc in NGC 4068. There is an apparent offset between the photometric and HI position angles. This twisting effect is also seen in the velocity field contours. The highest HI surface density is located in the southwest corner of the galaxy. Two other clumps of high HI surface density are seen to the northeast of this point. All three of these knots are coincident with clumps of  $H\alpha$ .

#### A6 NGC 4096

NGC 4096 is an SABc galaxy with a bright nucleus (de Vaucouleurs et al. 1964). Well-defined spiral arms combined with the effect of the high inclination ( $b/a = 0.267$ ) results in quickly-varying, bumpy radial profiles (Figure A16). A lopsidedness has been noted in the HI density profile and kinematics as well (García-Ruiz et al. 2002; van Eymeren et al. 2011). The HI data presented in Figure A18 was originally published in Richards et al. (2018). NGC 4096 is one of the redder galaxies in the sample, and it correspondingly has one of the highest median values of  $t_{YSP}$  from the radial component analysis at 2.3 Gyr.

#### A7 NGC 4214

NGC 4214 is another starbursting dwarf irregular galaxy. Previously studied multiwavelength observations revealed regions of the galaxy that are currently experiencing high levels of star formation (Huchra et al. 1983; Sargent & Filippenko 1991). The bright UV and  $H\alpha$  emission, noted in the literature, can also be seen in the radial profiles of Figure A19. The close proximity of this galaxy has also allowed resolved stellar population studies and CMD-derived SFHs (McQuinn et al. 2010; Weisz et al. 2011; Williams et al. 2011). The comparison between these SFH results and those of McQuinn et al. (2010) are discussed more in Section 5.1. The decreasing  $EW(H\alpha)$  profile in Figure A19 matches the expectations of starburst dwarf galaxies, but a B-R profile that grows more blue with radius matches the trend seen in larger spirals. Although this project does not quantify the steepness of the measured color gradients, doing this in the future may lead to exploring the connection between slope of color gradients, the age of stellar populations, and the masses of galaxies. In the case of NGC 4214, there is not a strong radial color gradient out to the low surface brightness and the galaxy appears to be dominated by an extremely young stellar population.

The HI distribution of NGC 4214 extends past the reach of the stellar component by a considerable amount (upper left panel of Figure A21). Clumps of UV emission are coincident with higher HI surface densities in the centre as well as along a weak bar structure. Bagetakos et al. (2011) documented 51 HI holes in NGC 4214, suggesting the scale height of this galaxy is low which would result in holes breaking out of the disc more easily than in other galaxies. Although there has been detailed studies of the extremely young ( $< 10$  Myr) stars in NGC 4214, there is still a prevalent old stellar population throughout the disc (Williams et al. 2011). The more evenly distributed older stars may be the reason that the radial SFHs do not show extremely young  $t_{YSP}$ 's everywhere ( $\langle t_{YSP} \rangle = 940$  Myr).

#### A8 NGC 4242

NGC 4242 is classified as an SAB(s)dm (RC3), with a low surface brightness disc (Eskridge et al. 2002). The B-R color and sSFR profiles for NGC 4242, shown in Figure 4, suggest a younger stellar population with heightened star formation exists at mid-galactic regions. The signature "U-shaped" B-R colour profile (i.e., with a minimum blue colour in the middle region) indicates a galaxy that may have undergone inside-out growth in addition to the substantial building up of an older stellar halo through accretion/mergers (Bakos et al. 2008; Dale et al. 2016).

Most of the HI is coincident with the stars, although there are detections of low surface density HI outside of the immediate region of the stellar disc (see Figure A22). The area of highest current star formation, as indicated by both the  $EW(H\alpha)$  profile and the SED-fitted SFH, is just within  $D_{25}$  (as shown as the white ellipse in the velocity field panel of Figure A22). The HI is mostly symmetric with only a slight extension to the southwest of the galaxy where the HI, as well as the  $H\alpha$ , extends further than the stellar population traced at  $3.6\mu\text{m}$ .

#### A9 NGC 4618

NGC 4618 is an SBm galaxy that forms a physical pair with NGC 4625. Bertola (1967) likened its morphology to the LMC because of its strong bar and its main arm that encompasses most of the central region. NGC 4618 has a bar that is not centered on the nucleus (Eskridge et al. 2002), and this offset can be seen in the photometric profiles in Figure A23. The tidal interaction between NGC 4618 and NGC 4625 is seen in the morphology and HI distributions of both (Figure A25). The asymmetry of NGC 4618 makes the radial analysis difficult to interpret, but was a good candidate for the individual stellar complex analysis. Staudaher et al. (2019) used the deep  $3.6\mu\text{m}$  image of NGC 4618 to quantify the breaks in the stellar disc, finding a bulge and possible four disc components. A complicated evolutionary history, whether through stellar migration, tidal interactions, mergers, or some mixture of all these factors, may be an explanation for the changes in NGC 4618's stellar disc.

#### A10 NGC 4625

NGC 4625 was one of the first galaxies to be classified as having an extended UV (XUV) disc (Gil de Paz et al. 2005; Thilker et al. 2007). The UV and  $H\alpha$  emission that persists far outside of  $D_{25}$  combined with elevated HI surface densities (Figure A25) and young  $t_{YSP}$ 's (Figure A27) in the same region points to late stage disc growth (Elmegreen & Hunter 2006; Bush et al. 2014). According to the color profile (Figure A26) and the radial SFHs (Figure A27), the oldest stellar population in NGC 4625 resides near the  $D_{25}$  isophote. Because of the clear difference between its inner and outer regions, NGC 4625 is a prime example of a galaxy with an "inside-out" growth signature.

#### A11 NGC 7793

NGC 7793 is an SAd galaxy with very little structure in its old stellar disc and is part of the Sculptor group (Elmegreen & Elmegreen (1984). Because of its close proximity to the Milky Way, NGC 7793 has been extensively studied in many wavelengths. The photometry in Carignan (1985) as well as the measurements in Figure A28 show little to no color gradient across the galaxy. The SED-derived radial SFH of NGC 7793 (Figure A29) shows how NGC 7793 has a roughly



constant SFH over its lifetime with the exception of the small bulge region, as mentioned in Section 5.1 and in [Sacchi et al. \(2019\)](#). The similar results among all annuli included in the radial analysis suggests that the continuous SFH was experienced across the galaxy, and not limited to either the inner or outer regions. The HI velocity field of NGC 7793 is relatively symmetric, with the exception of the low density southeast region (Figure A30). The HI disc does not extend much more than the stellar disc at  $3.6\mu$ , agreeing with the assessment of [de Blok et al. \(2008\)](#).

#### A12 UGC 07408

UGC 07408 has weakly detected  $H\alpha$  emission, has very little HI content ([Swaters et al. 2002](#)), and has only a moderate blue-to-red color gradient ([Hunter & Elmegreen 2006](#)). The inner regions do not change rapidly in B-R, which is reflected in the cumulative SFH. The two inner most regions are identical in their SFHs. Between the two inner regions and the next annulus, there is a larger change in  $t_{ySP}$  (Figure A32) than would be suggested by the photometric diagnostics of Figure A31. The strong, recent burst suggested by the results in the central regions would most likely lead to some current star formation, which goes undetected by the  $H\alpha$  image. This contradiction leads us to conclude that the results for UGC 07408 may be overestimating the burst fraction,  $f_{burst}$ . The HI observations come from WHISP and are shown in Figure A33.

#### A13 UGC 07577

UGC 07577 (DDO 125) is a low mass dwarf irregular galaxy that is often associated with NGC 4449 (physical separation of 40 kpc) ([Barnes & Hernquist 1992](#)). UGC 07577 lacks a dominant dark matter component and could have formed in the tidal streams of NGC 4449 ([Swaters 1999](#); [Hunter et al. 2000](#)). Figures A34 and A35 show a galaxy experiencing elevated star formation in the central regions. An analysis of its global star formation history ([Weisz et al. 2011](#)) suggested that the majority (~90%) of the current fraction of stars in the galaxy was formed more than 6 Gyrs ago. The rest of the stars were formed within the past 1 Gyr. The SED-derived SFHs in Figure A35, therefore, may have overestimated  $f_{burst}$ . However, the SED-derived  $t_{ySP}$  at every radii is less than 1 Gyr. A galaxy that may be experiencing its first large star formation episode in several Gyr may be especially suited for the double exponential SFH parametrization. The HI observations shown in Figure A36 were previously published in [Hunter et al. \(1998\)](#). The velocity field shows solid body rotation that is undisturbed.

#### A14 UGC 07608

UGC 07608 (DDO 129) is an irregular galaxy with bright UV sources in the north west region of the galaxy (upper right panel of Figure A39). Its irregular morphology made UGC 07608's azimuthally averaged photometry appear bumpy, seen in Figure A37 and previously seen with the photometry in [Patterson & Thuan \(1996\)](#). However, the coarser placement of ellipses for the SED fitting analysis makes the knots and clumps of  $H\alpha$  and UV emission become less apparent (Figure A38). The high  $EW(H\alpha)$  coupled with the rather blue colors seen in UGC 07608 are correlated with the high  $f_{burst}$  and low  $t_{ySP}$  in the cumulative SFHs in all annuli.

#### A15 UGC 08320

UGC 08320 (DDO 168) is a well-studied dwarf irregular in the Canes Venatici I group ([Karachentsev et al. 2003](#)). [Bremnes et al. \(1999\)](#) notes a luminosity excess above a pure exponential disc at large radii in the surface brightness profile of this dwarf. Although there are clear breaks in the surface brightness profiles of Figure A40, a closer look at how the profiles deviate from an exponential fit would be needed to confirm that the methods used in this project produce the same result as [Bremnes et al. \(1999\)](#).

The SFH results for UGC 08320 are similar to those of [Dale et al. \(2016\)](#), even with slightly differing SED parameters spaces. A large portion of the stellar population formed more recently than most of the other galaxies in this sample, according to the SFH results in Figure A41. The oldest stellar population, residing in the outermost annulus, still has undergone recent star formation. This display of an extremely recent, large onset of star formation, coinciding with the extended HI disc ([Ghosh & Jog 2018](#)) and a slow HI bar ([Patra & Jog 2019](#)), points to a galaxy going through an important evolutionary phase.

The HI extends past the stellar component by many arcseconds (Figure A42). The HI surface density contours and velocity field appears twisted, suggesting a warped disc. The low density HI coincides with the reddest stellar populations in the galaxy measured by the color gradients,  $\log(sSFR)$  profile,  $EW(H\alpha)$  profile, SED-derived SFH (Figures A40 and A41). There is a misalignment of the stellar and HI position angles.

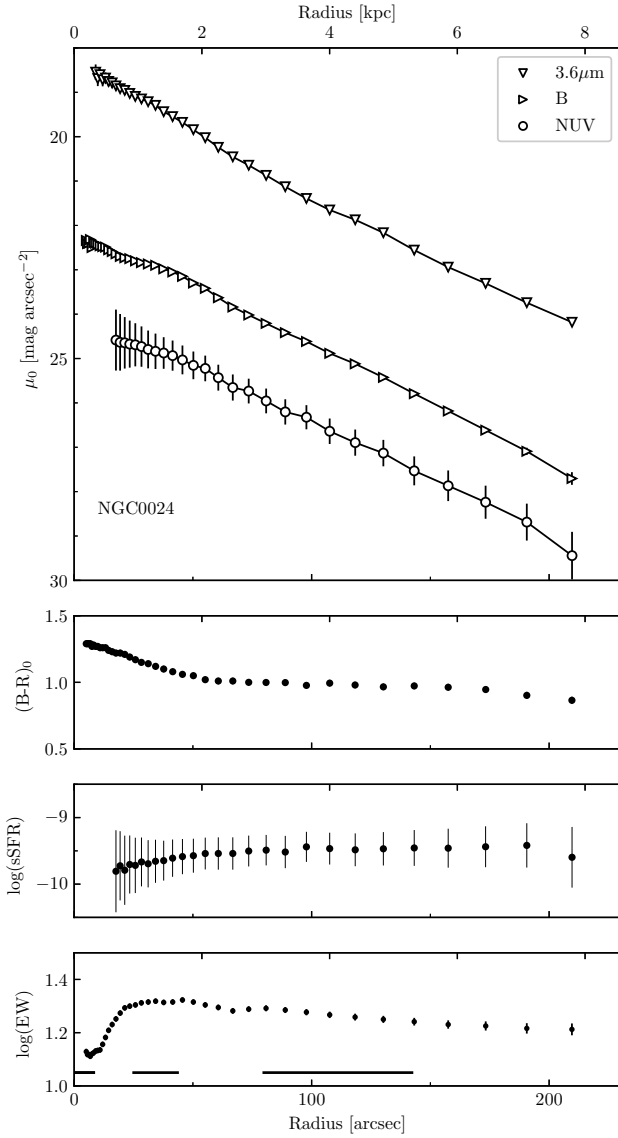


**Figure A1.** The photometric and classical SFR tracer profiles for NGC 0024. Profiles are corrected for foreground extinction and inclination. In the bottom panel, solid horizontal lines are used to show the larger radial bins used for SED fitting.

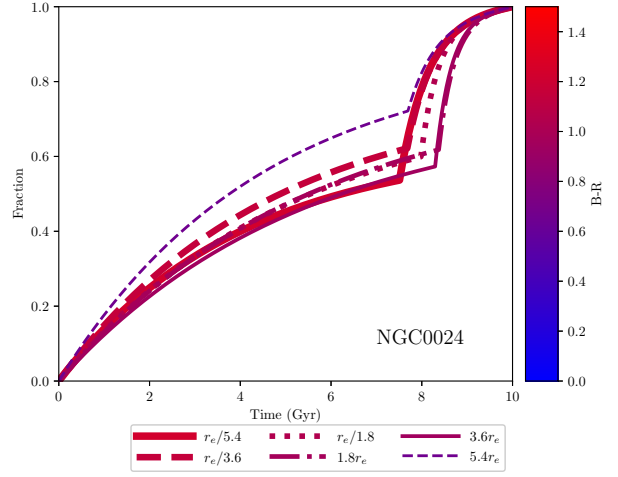


**Figure A2.** The cumulative SFH for radial bins in NGC 0024. The central region is a 6'' aperture. All radii are measured along the major axis. Any radial bin that is present in the legend but not in the figure means that the SED fitting resulted in a fit with  $\chi^2_{\nu} > 15$  for that bin.

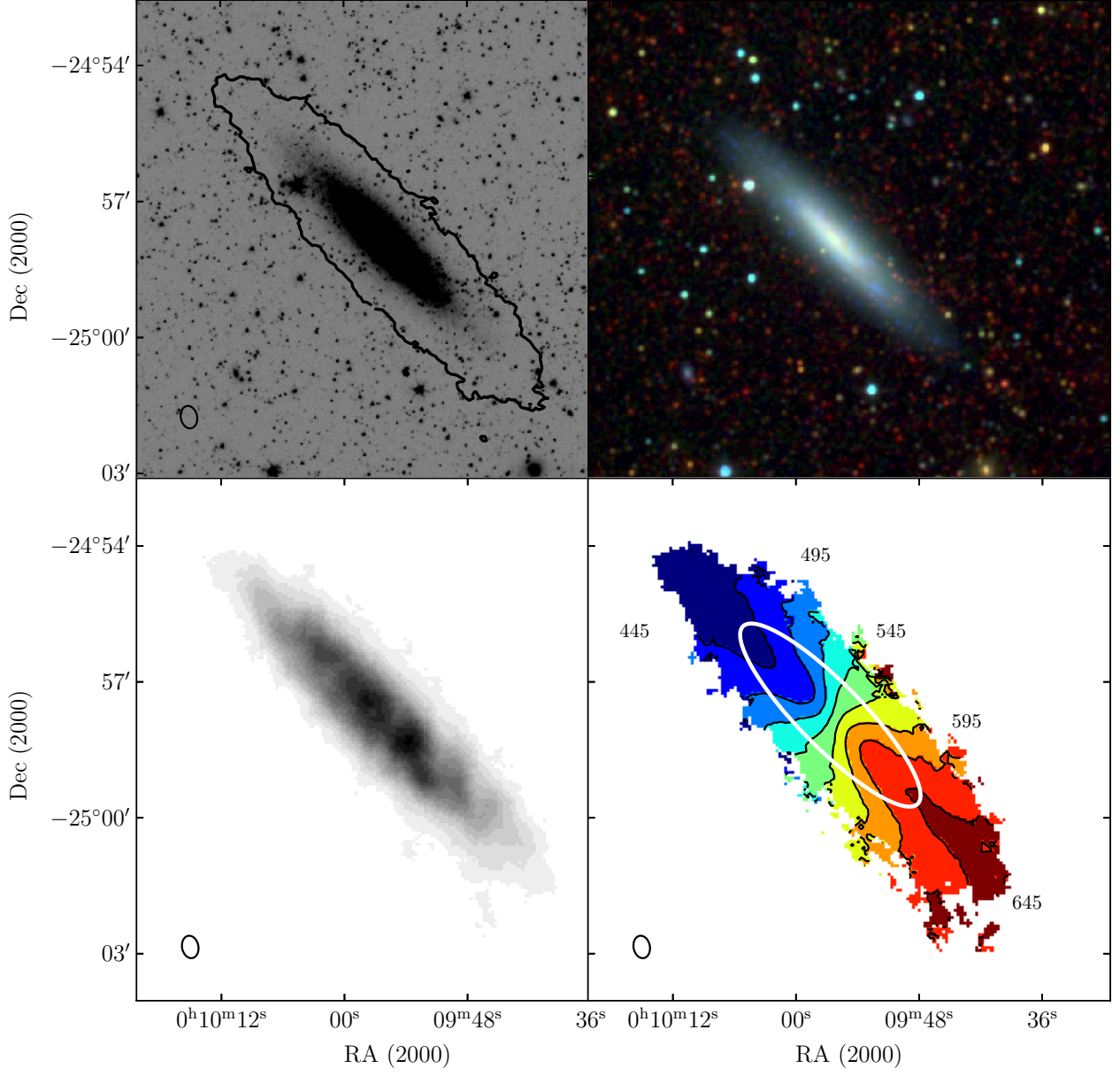


**Figure A3.** NGC 0024. Top left panel shows the extent of the HI distribution (contour) in relation to the underlying stellar disc ( $3.6\ \mu\text{m}$  image). Top left panel shows an RGB image where red is  $3.6\ \mu\text{m}$ , green is R from WIYN, and blue is B + FUV from WIYN/Galex. Bottom left panel shows the HI surface density contours starting at  $0.5 \times 10^{20}\ \text{atoms cm}^{-2}$ . The bottom right panel shows the HI velocity field.

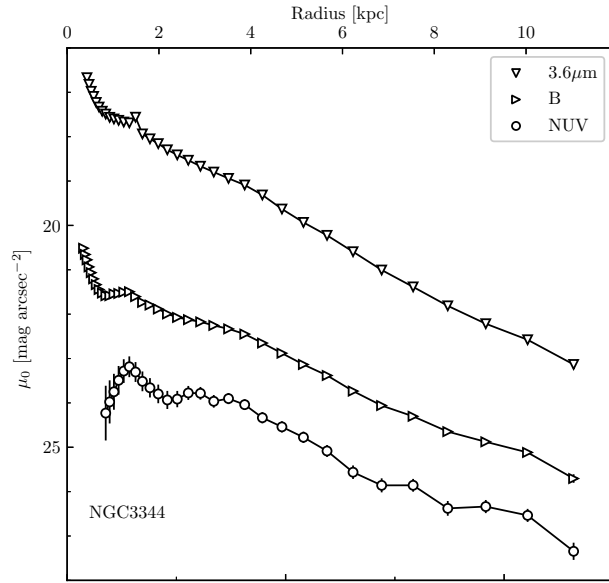


**Figure A4.** NGC 3344: Panels same as Figure A1.

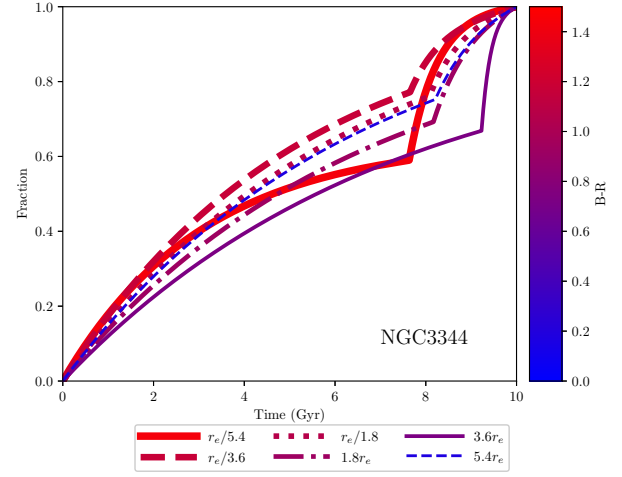


**Figure A5.** NGC 3344 : Plot same as Figure A2.



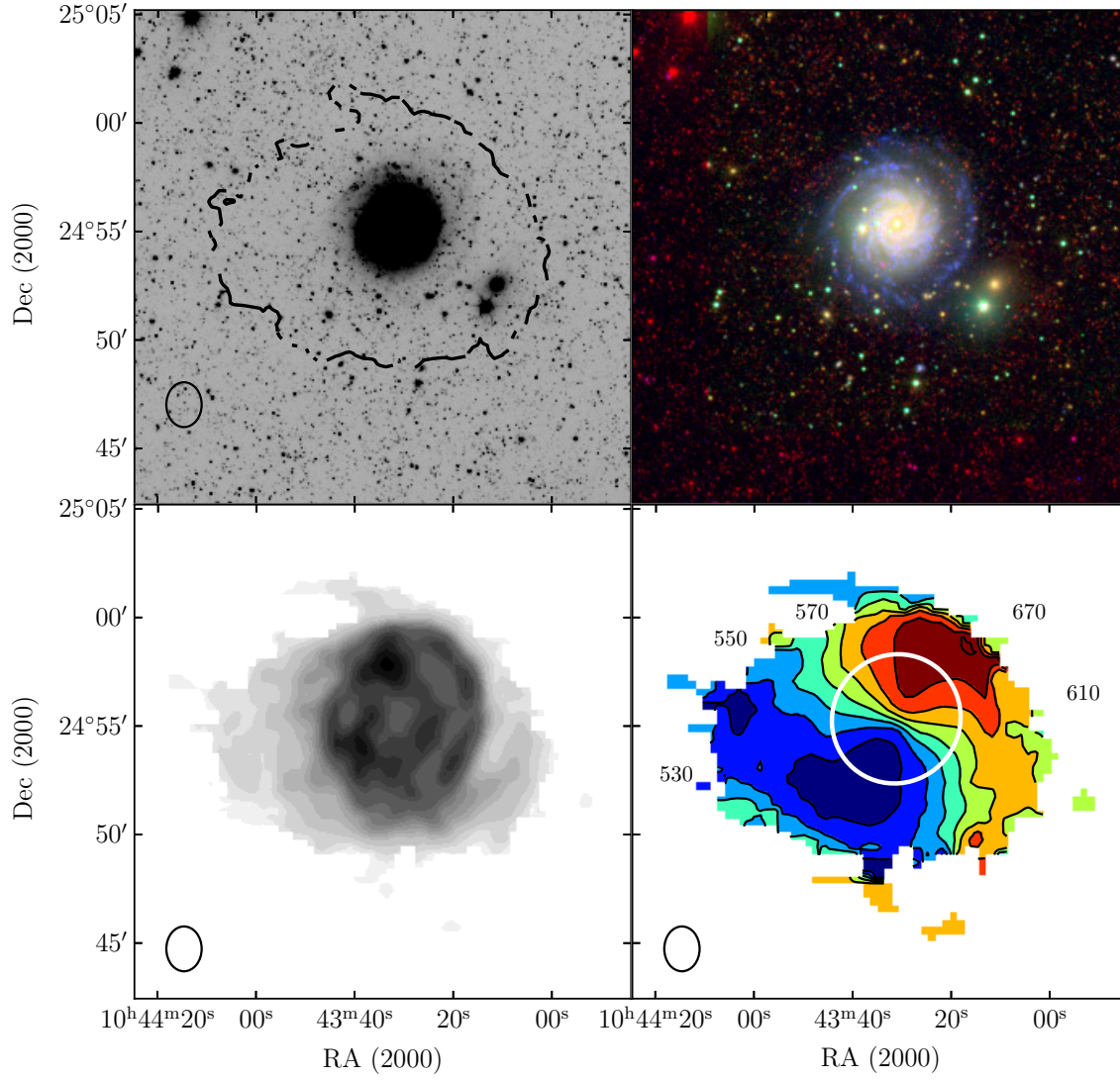


**Figure A6.** NGC 3344: Panels same as Figure A3.

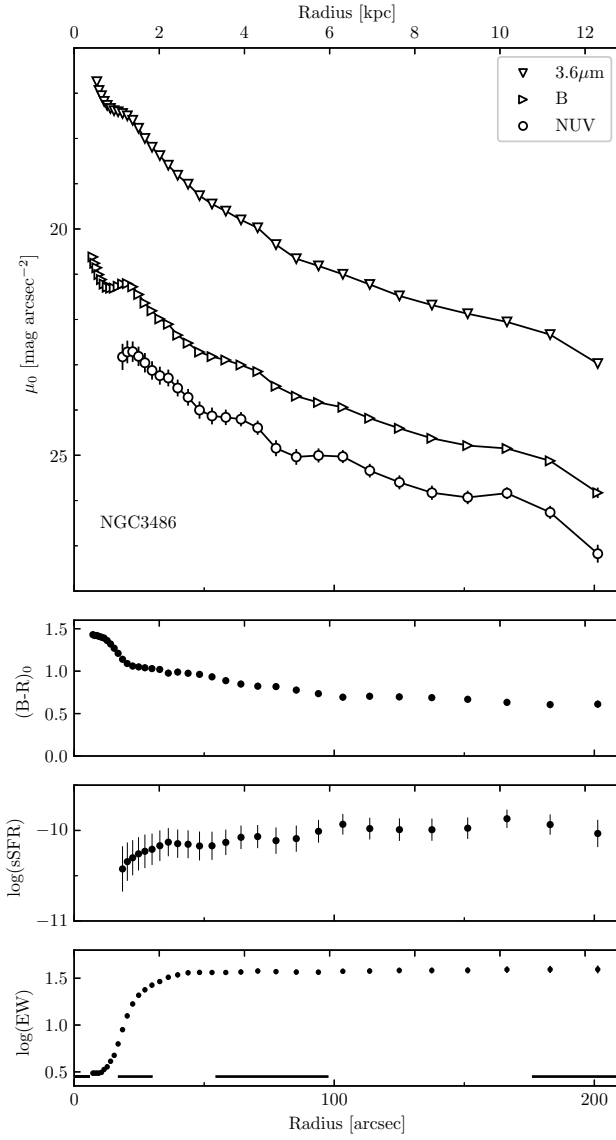


**Figure A7.** NGC 3486: Panels same as Figure A1.

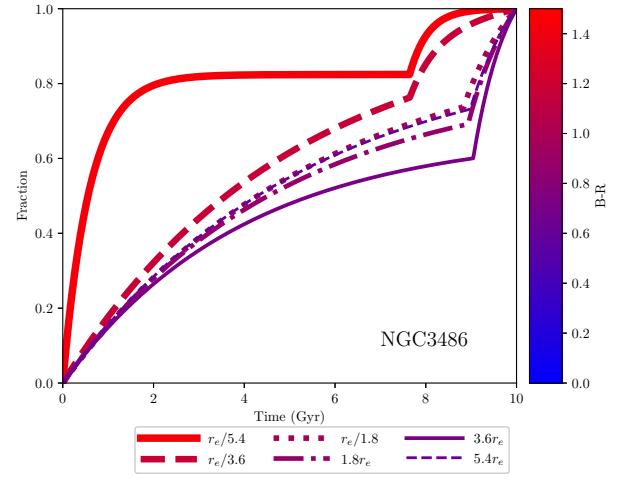


**Figure A8.** NGC 3486 : Plot same as Figure A2.

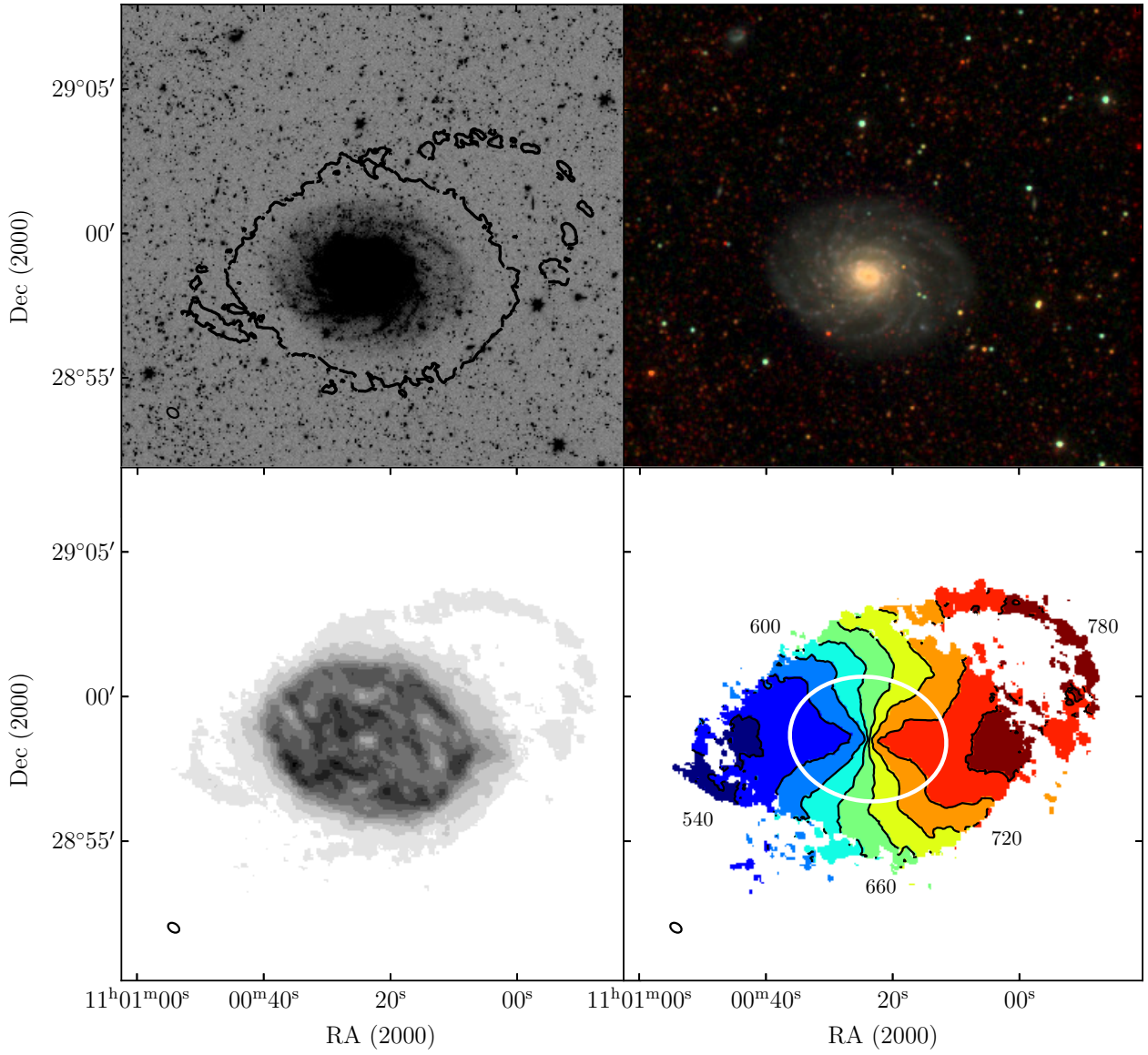


**Figure A9.** NGC 3486: Panels same as Figure A3.

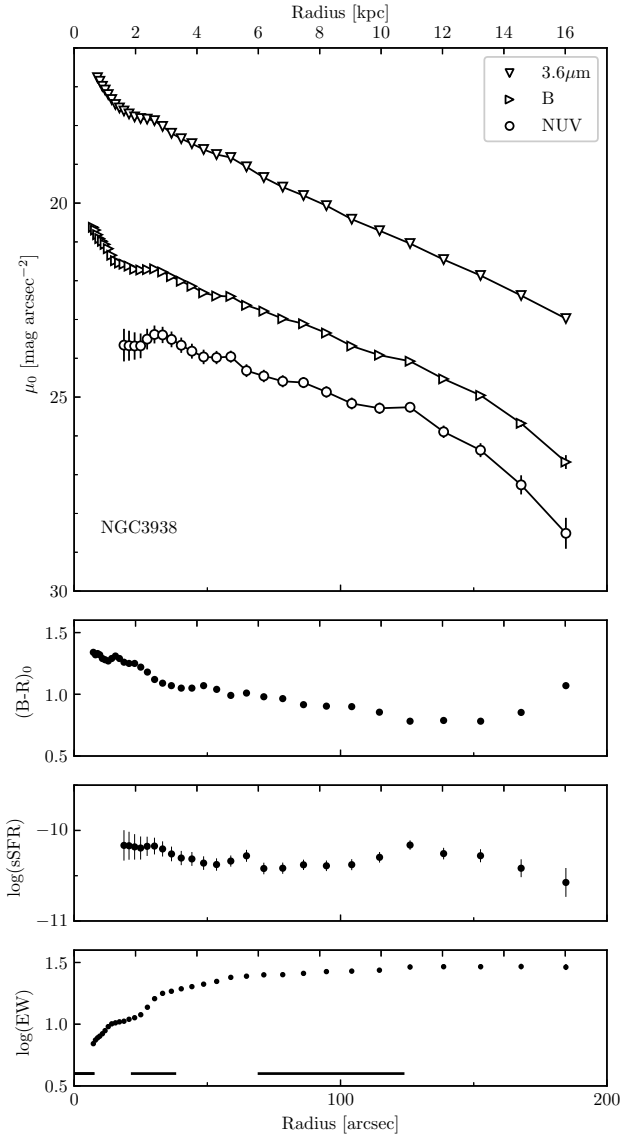


**Figure A10.** NGC 3938 : Panels same as Figure A1.

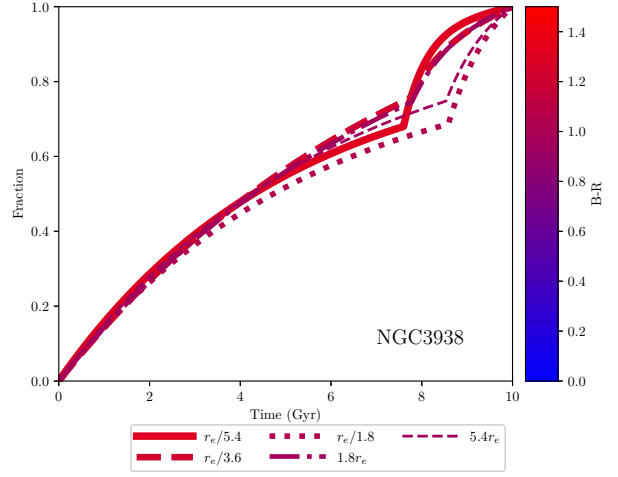


**Figure A11.** NGC 3938 : Plot same as Figure A2.



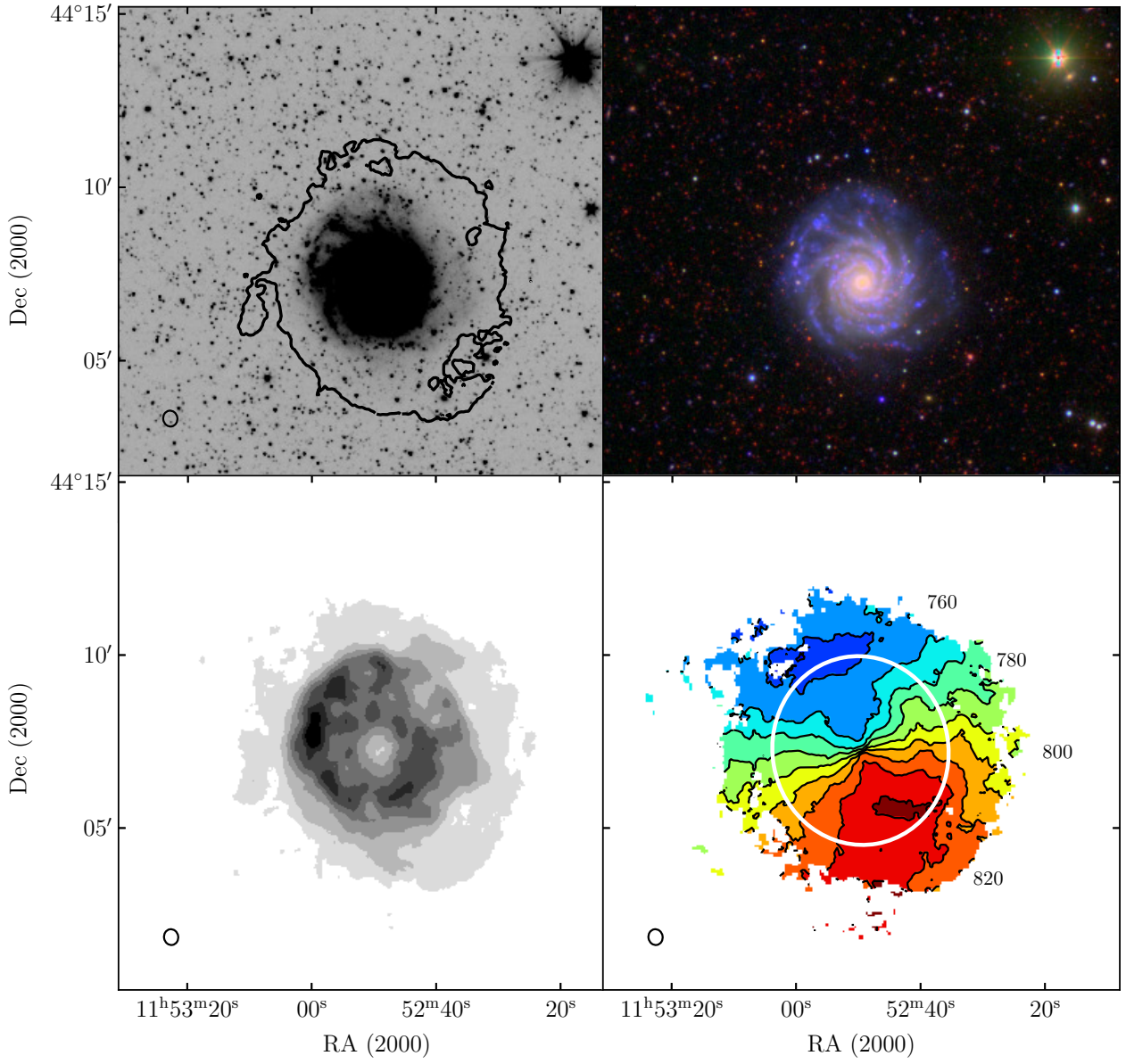


**Figure A12.** NGC 3938 : Panels same as Figure A3.

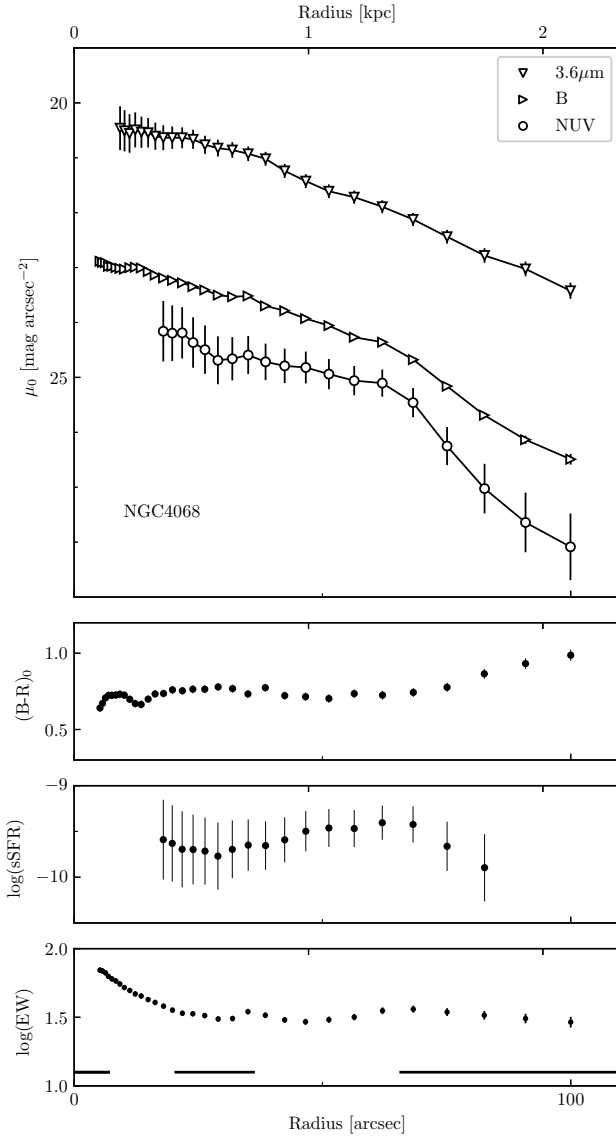


**Figure A13.** NGC 4068: Panels same as Figure A1.

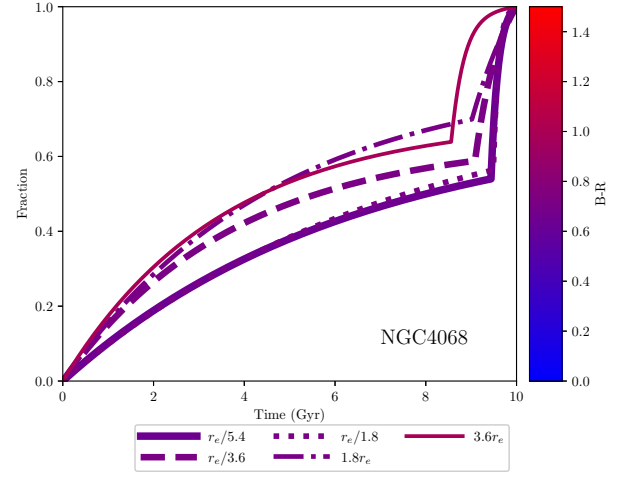


**Figure A14.** NGC 4068 : Plot same as Figure A2.

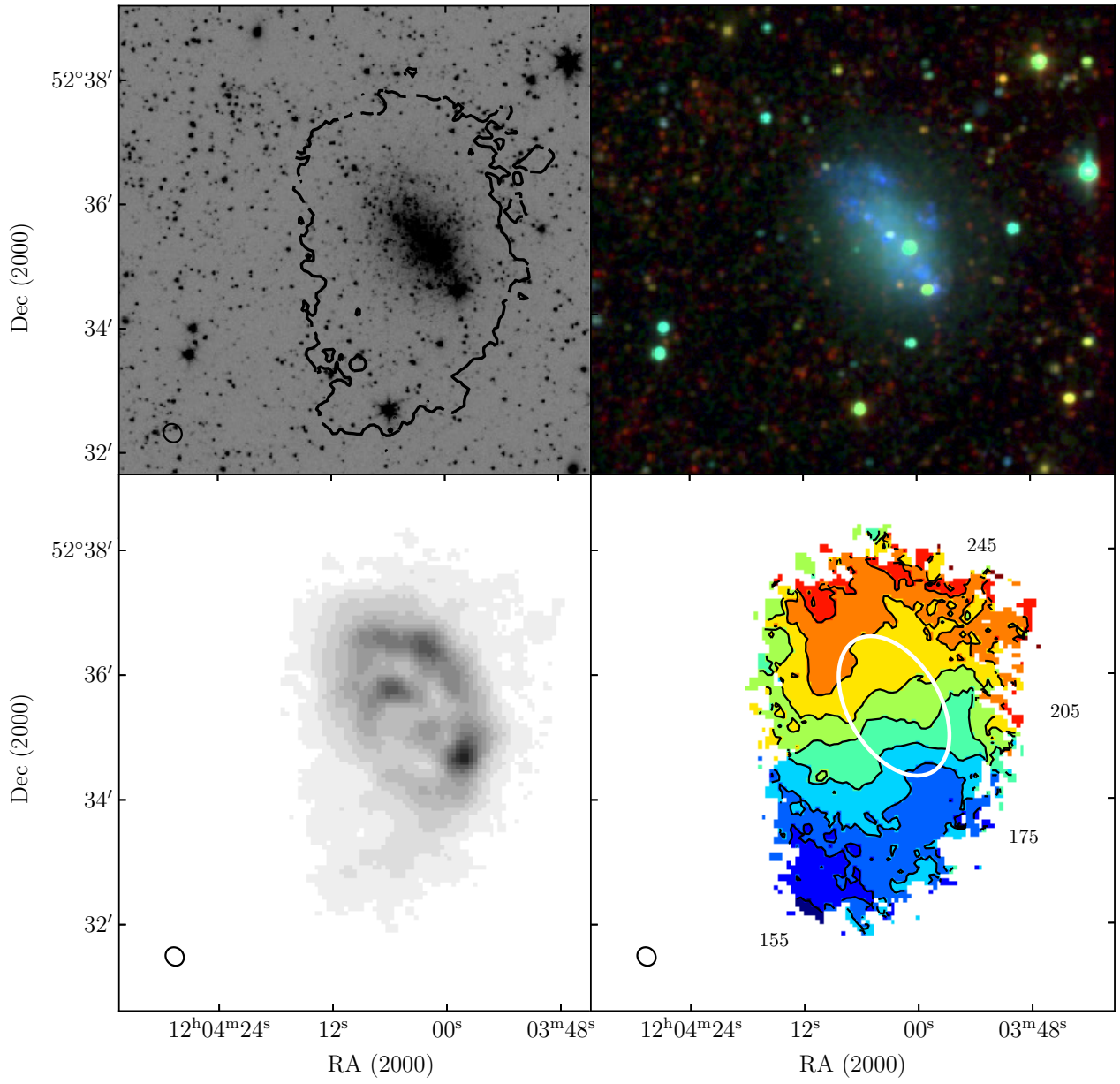


**Figure A15.** NGC 4068: Panels same as Figure A3.

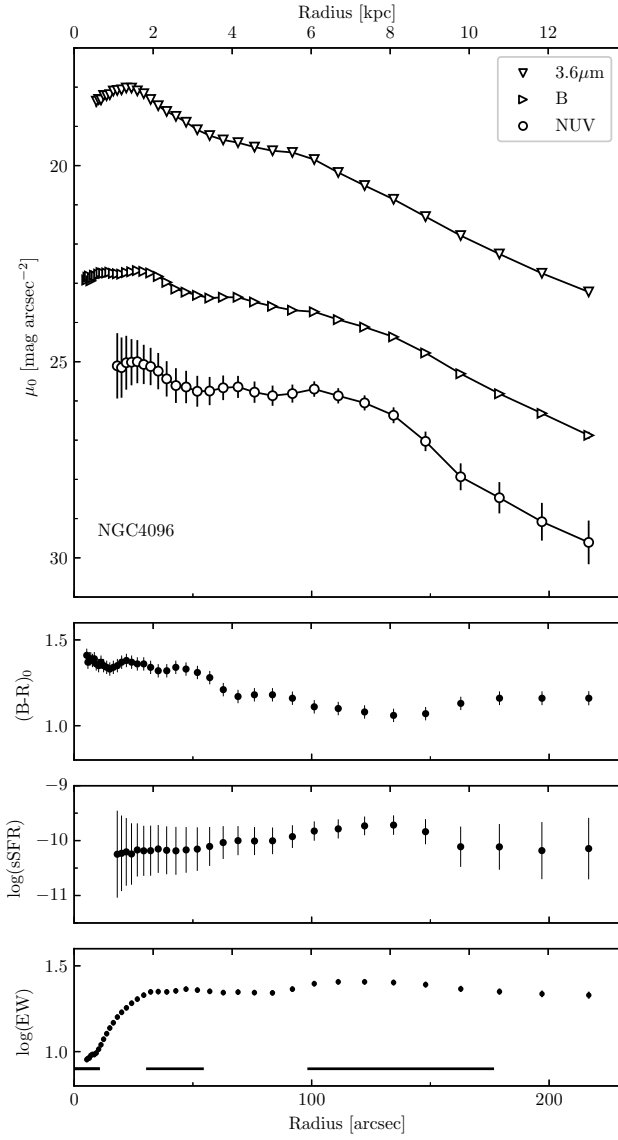


**Figure A16.** NGC 4096: Panels same as Figure A1.

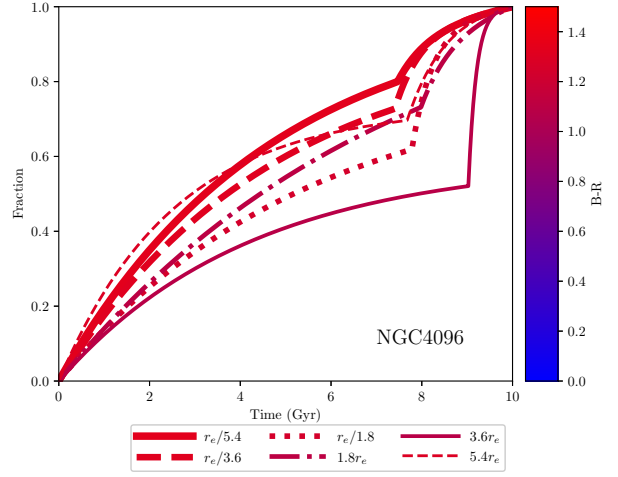


**Figure A17.** NGC 4096 : Plot same as Figure A2.



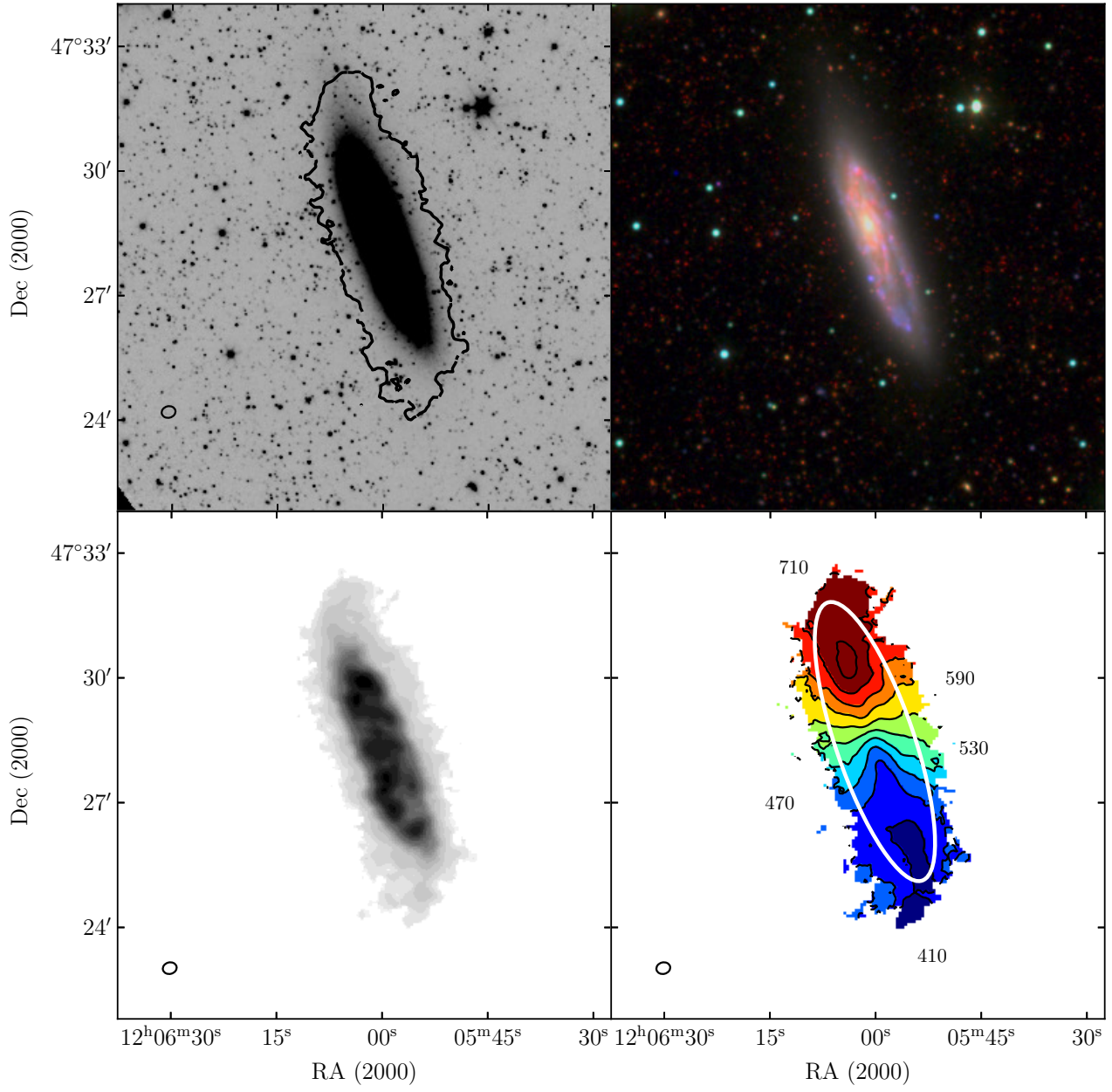


**Figure A18.** NGC 4096: Panels same as Figure A3.

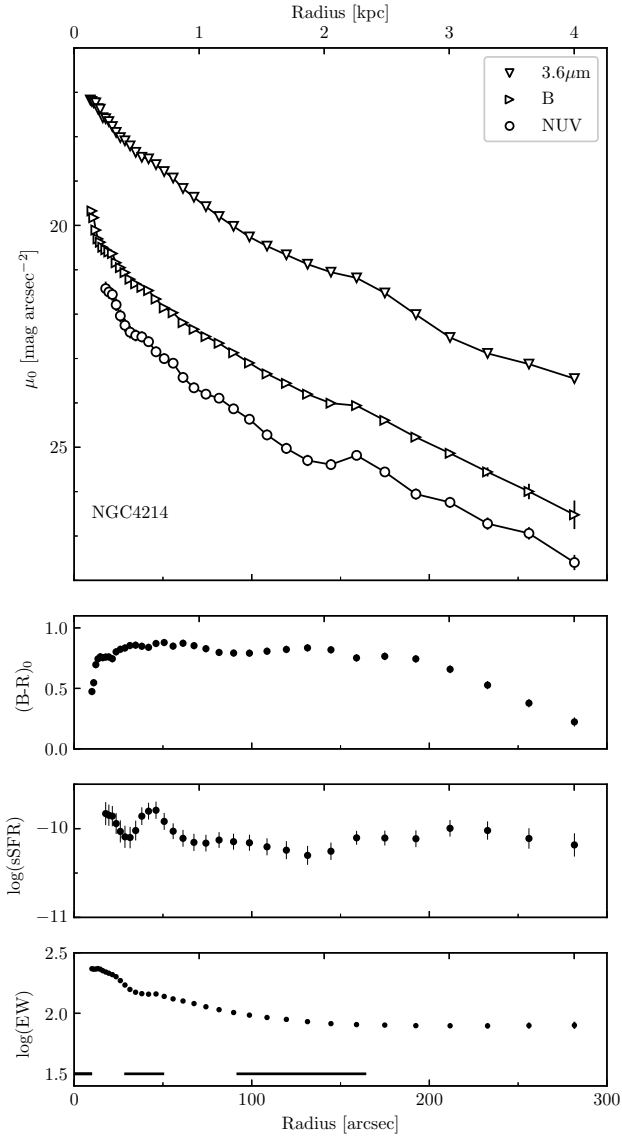


Figure A19. NGC 4214: Panels same as Figure A1

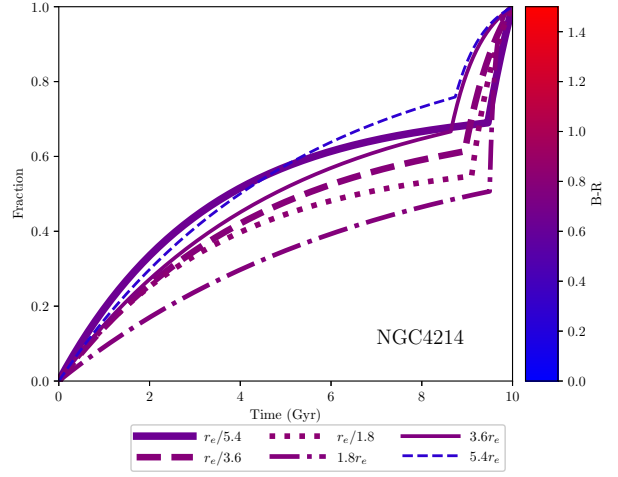
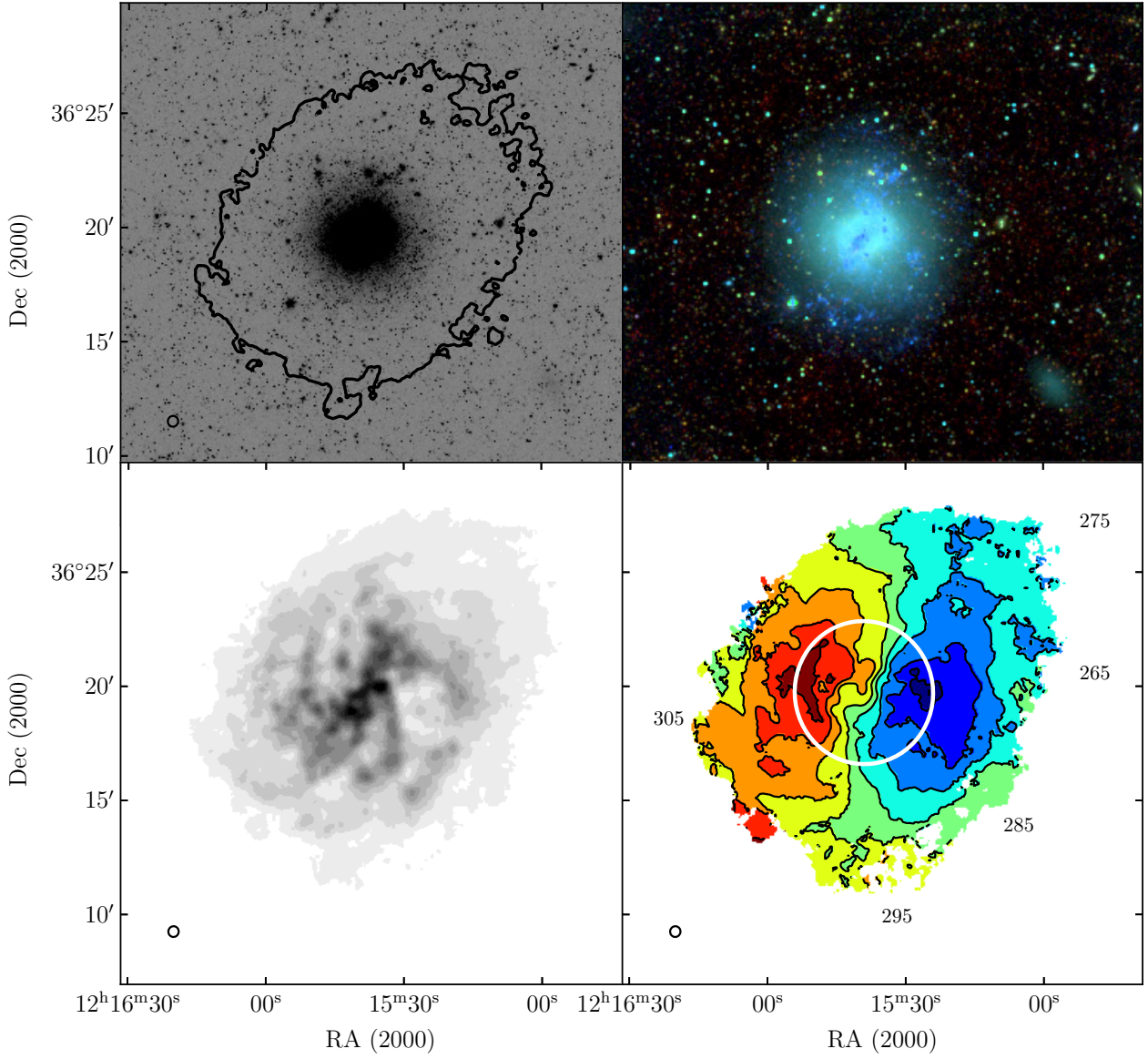
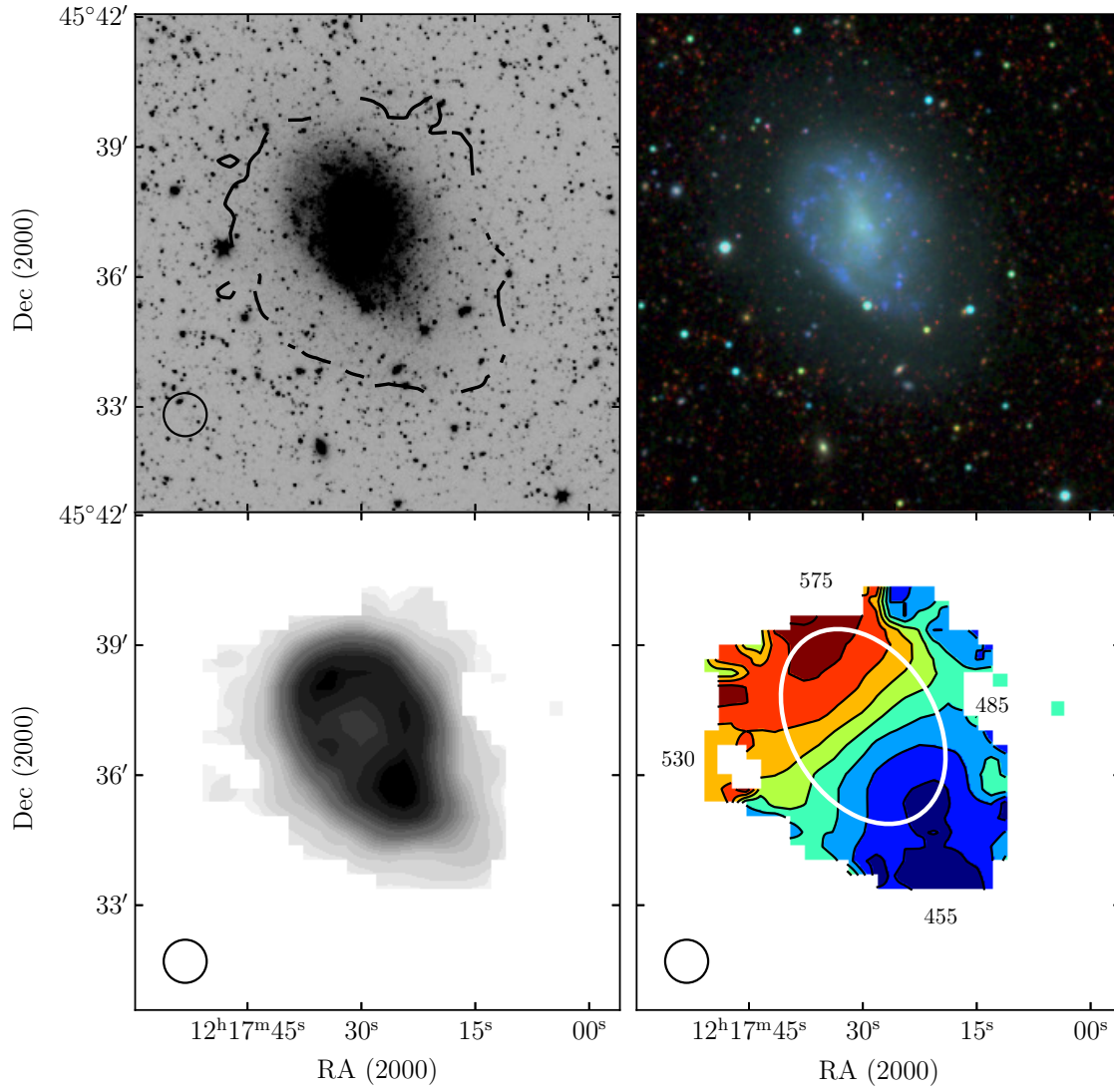


Figure A20. NGC 4214 : Plot same as Figure A2.



**Figure A21.** NGC 4214: Panels same as Figure A3.



**Figure A22.** NGC 4242: Panels same as Figure A3.

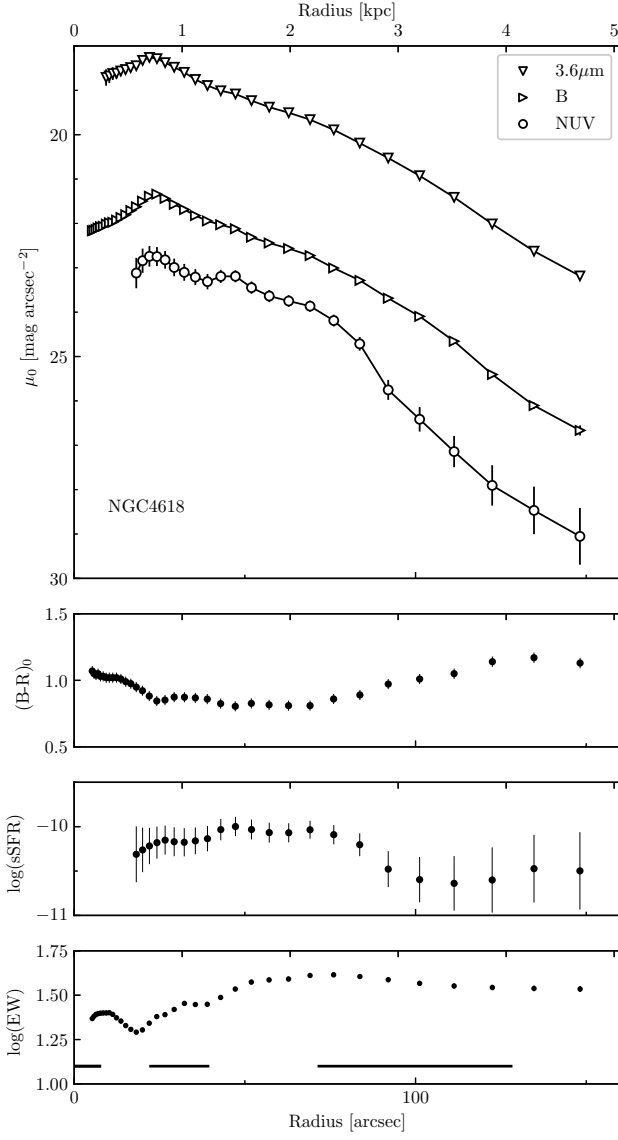


**Figure A23.** NGC 4618: Panels same as Figure A1.

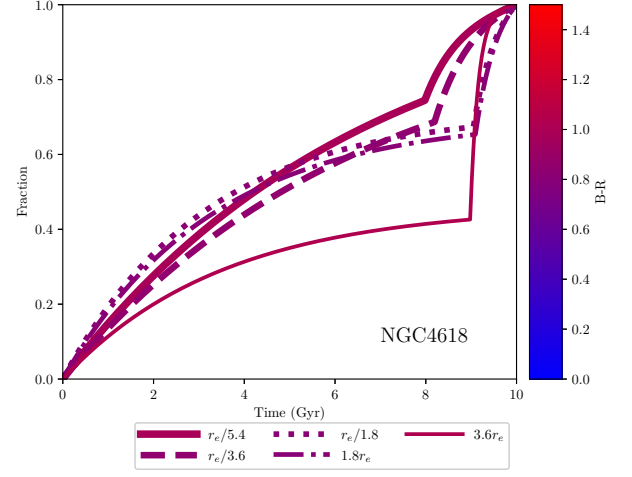


**Figure A24.** NGC 4618 : Plot same as Figure A2.



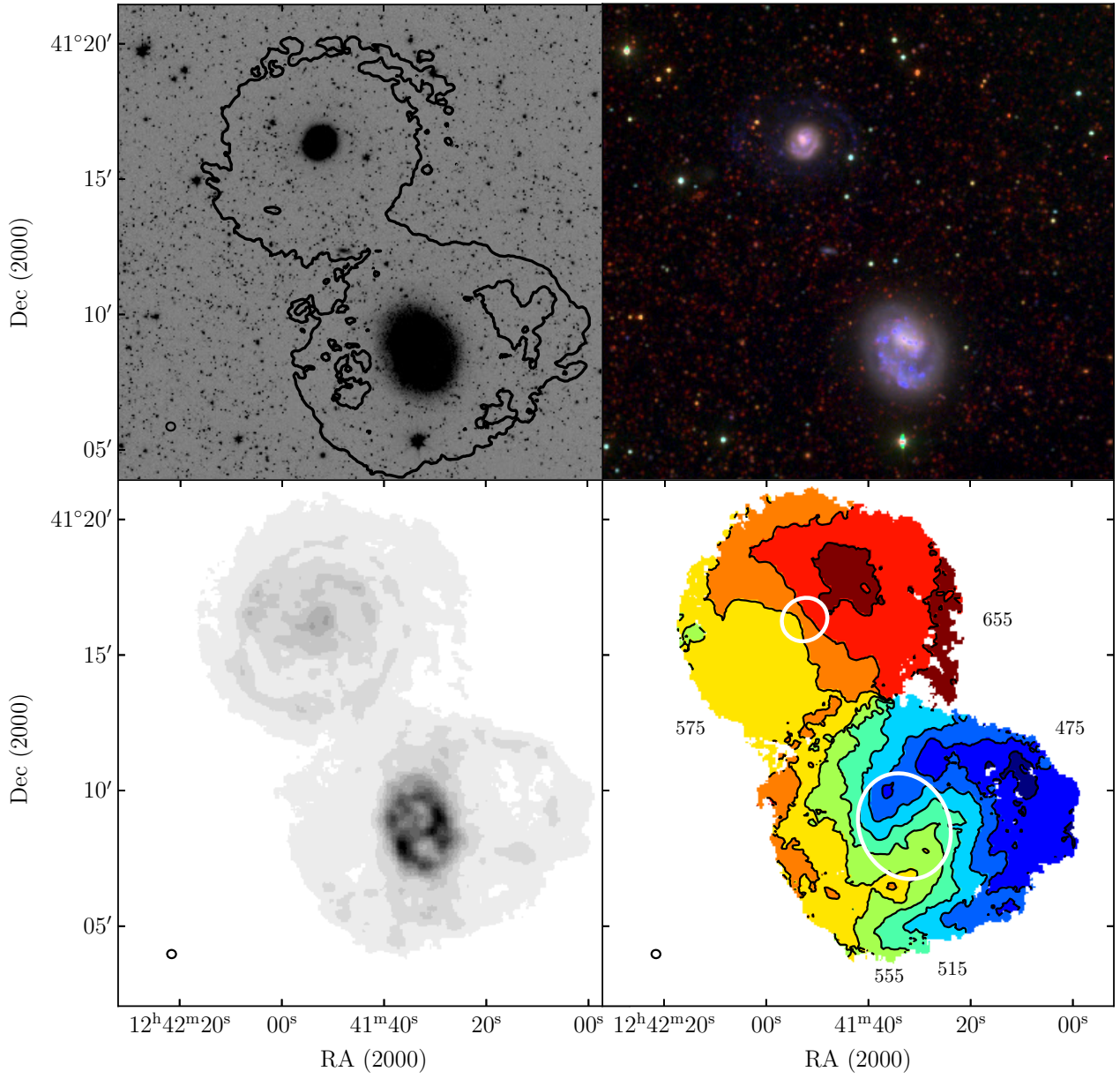


**Figure A25.** NGC 4618 & NGC4625: Panels same as Figure A3.

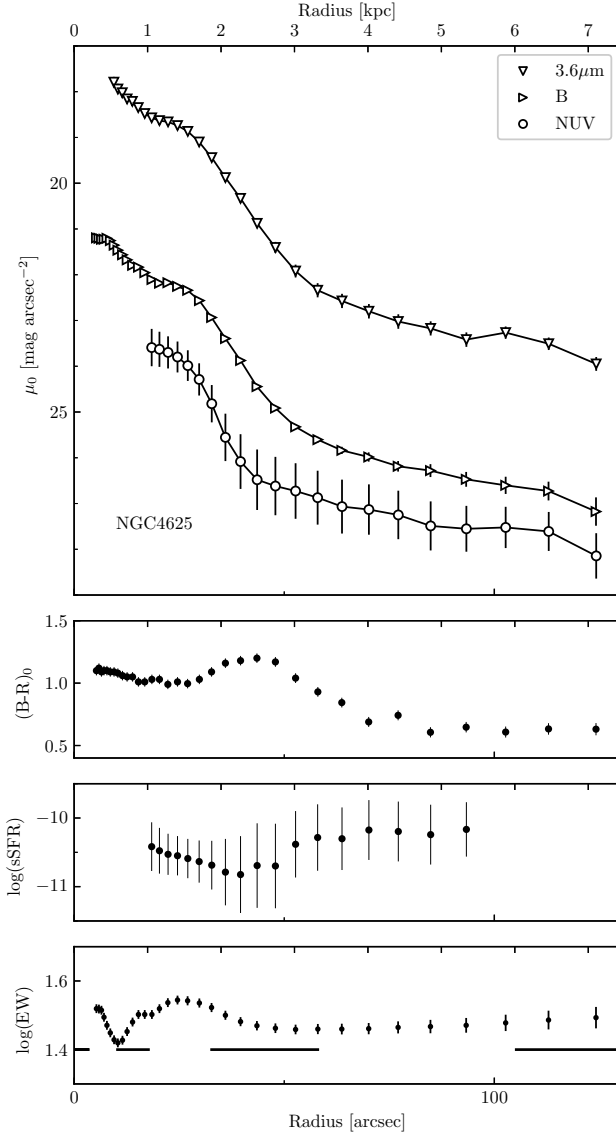


**Figure A26.** NGC 4625: Panels same as Figure A1.

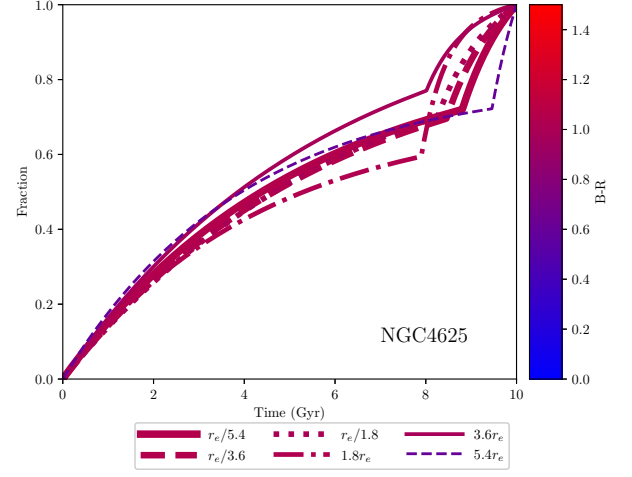


**Figure A27.** NGC 4625 : Plot same as Figure A2.

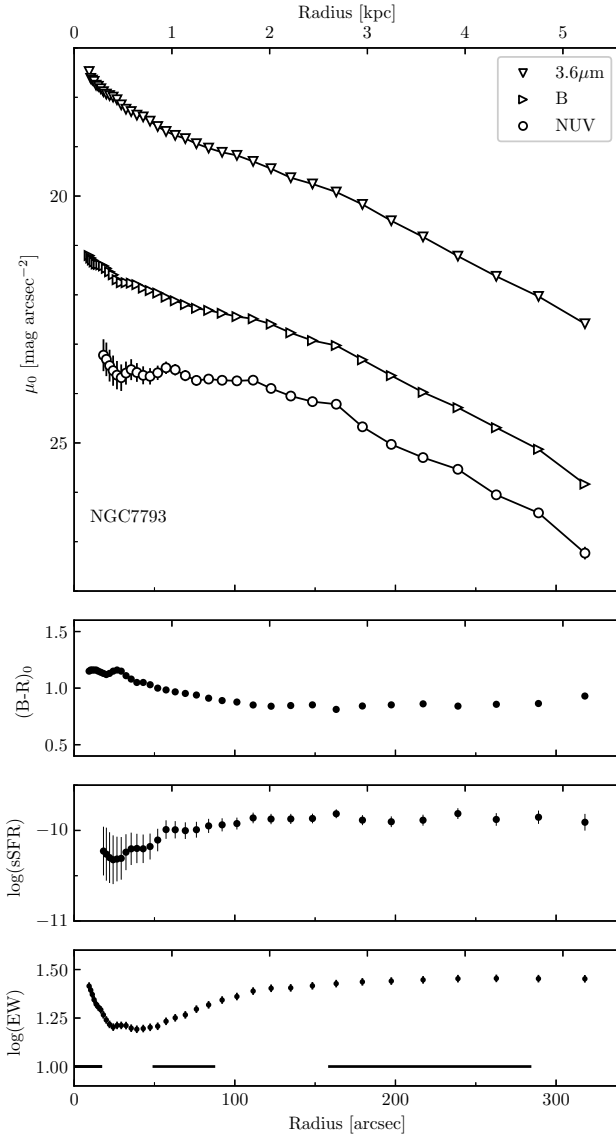


**Figure A28.** NGC 7793: Panels same as Figure A1.

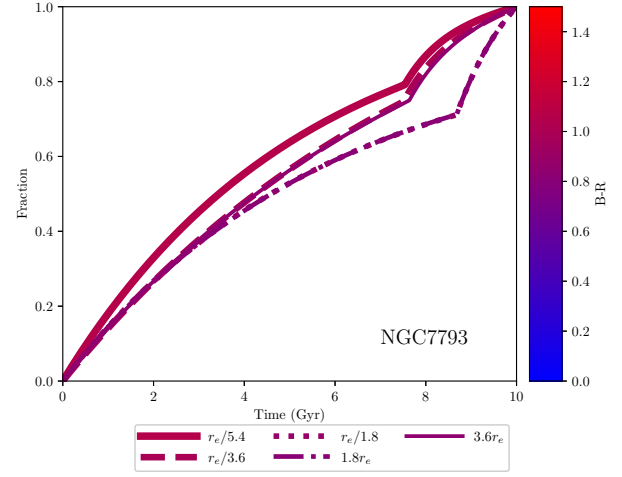


**Figure A29.** NGC 7793 : Plot same as Figure A2. The results of NGC 7793 are compared to the CMD-derived SFH in Section 5.1.

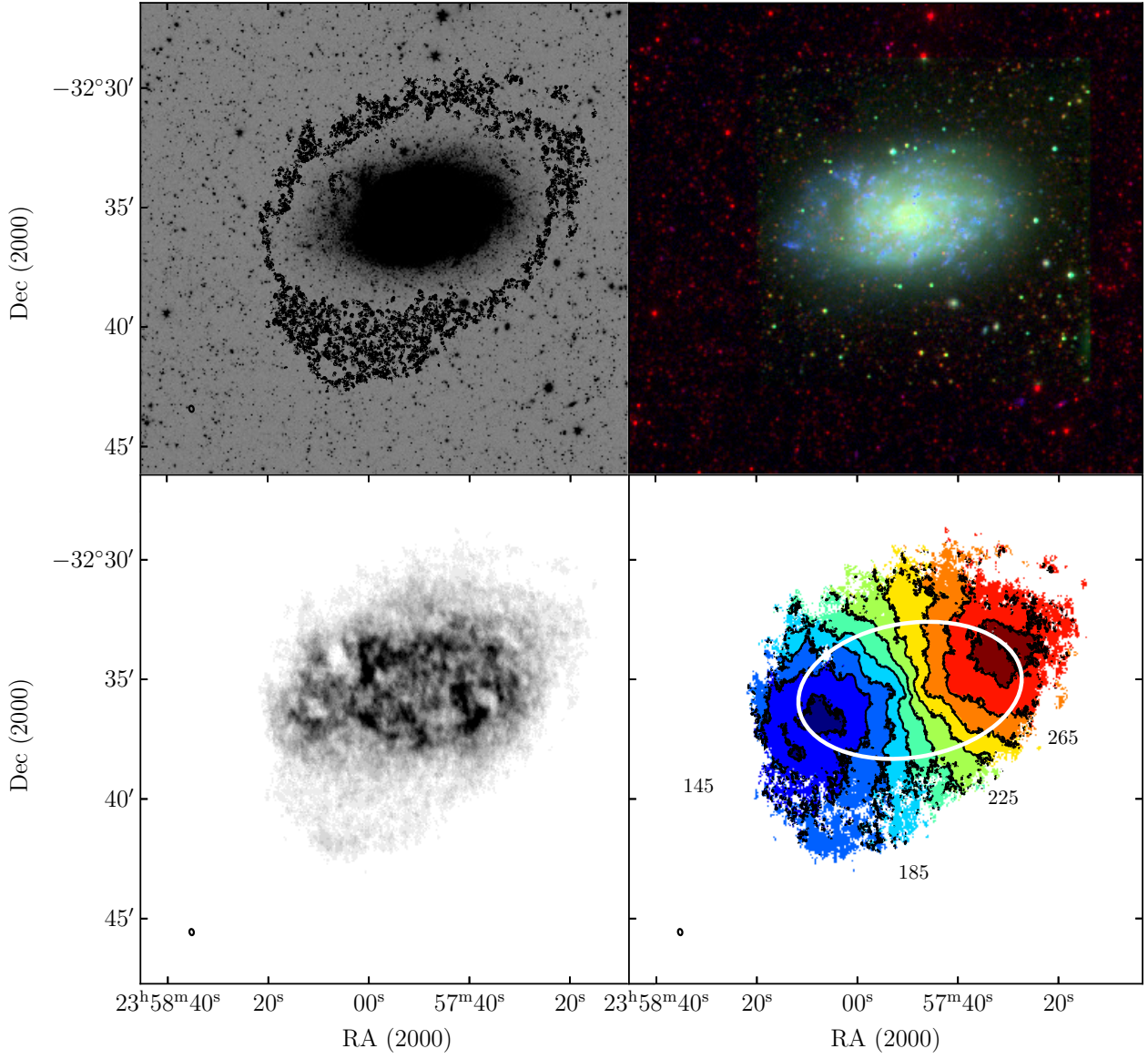


**Figure A30.** NGC 7793 : Panels same as Figure A3.

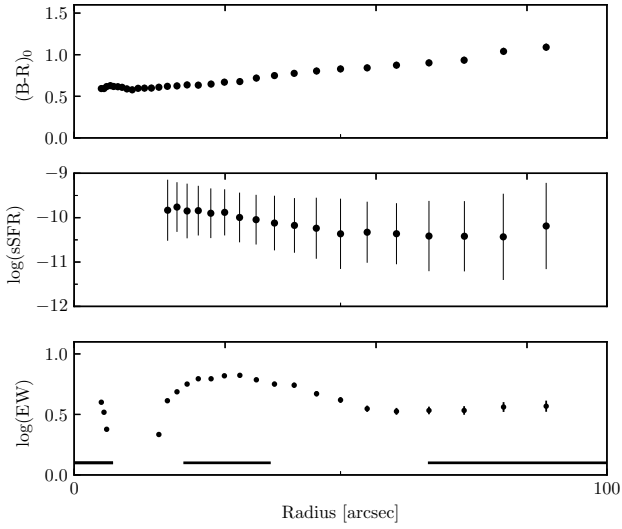
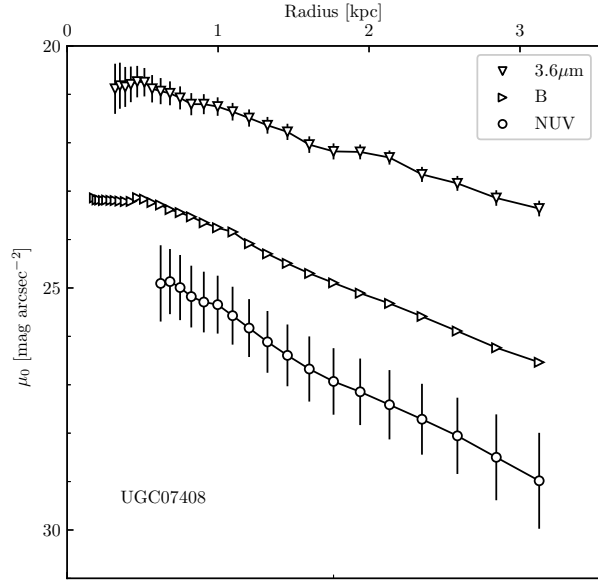


**Figure A31.** UGC 07408 : Panels same as Figure A1.

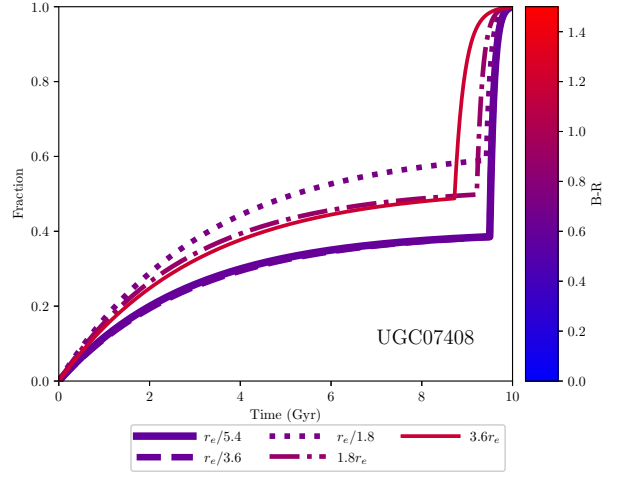


**Figure A32.** UGC 07408 : Plot same as Figure A2.



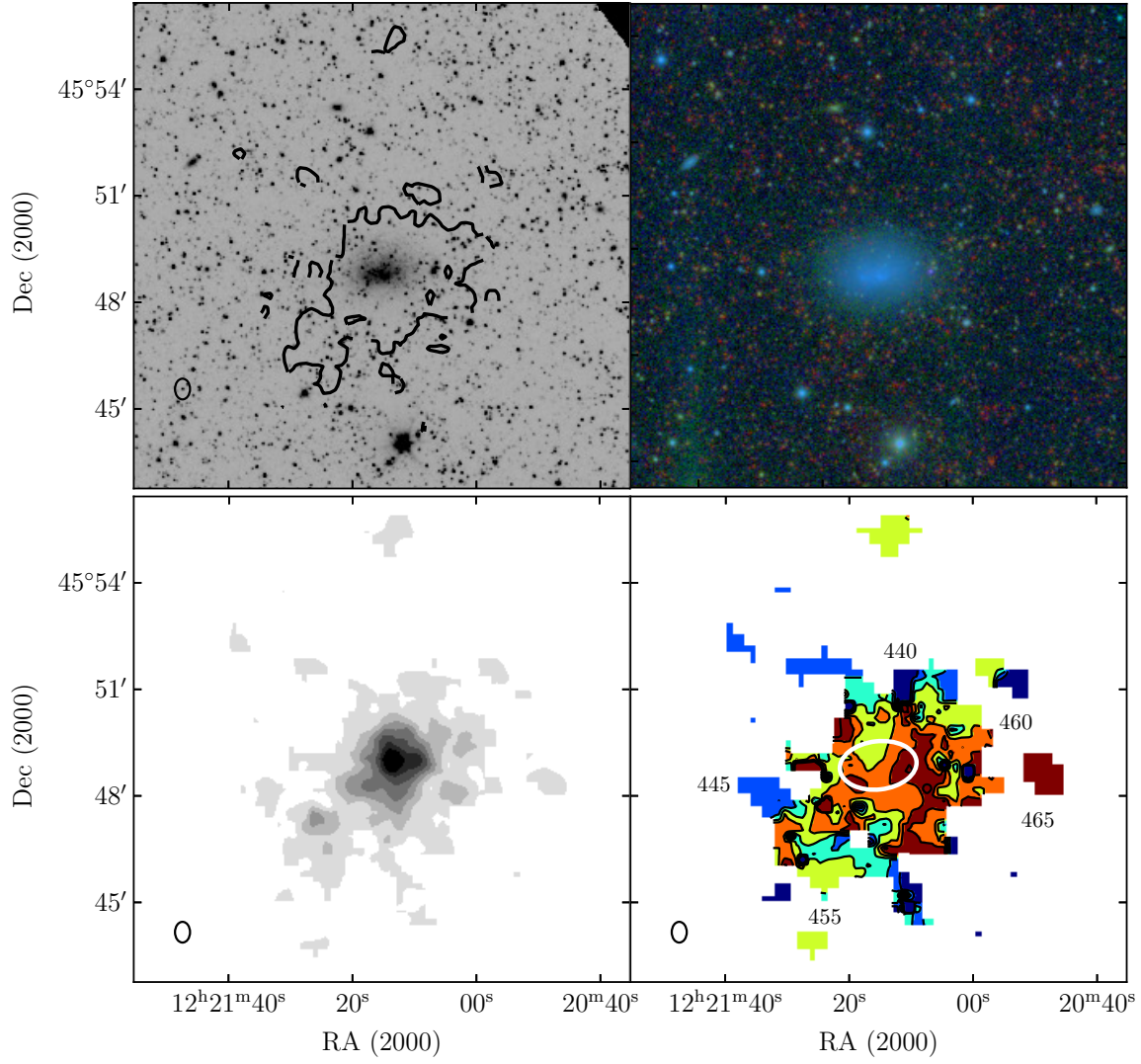


**Figure A33.** UGC 07408 : Plot same as Figure A3.

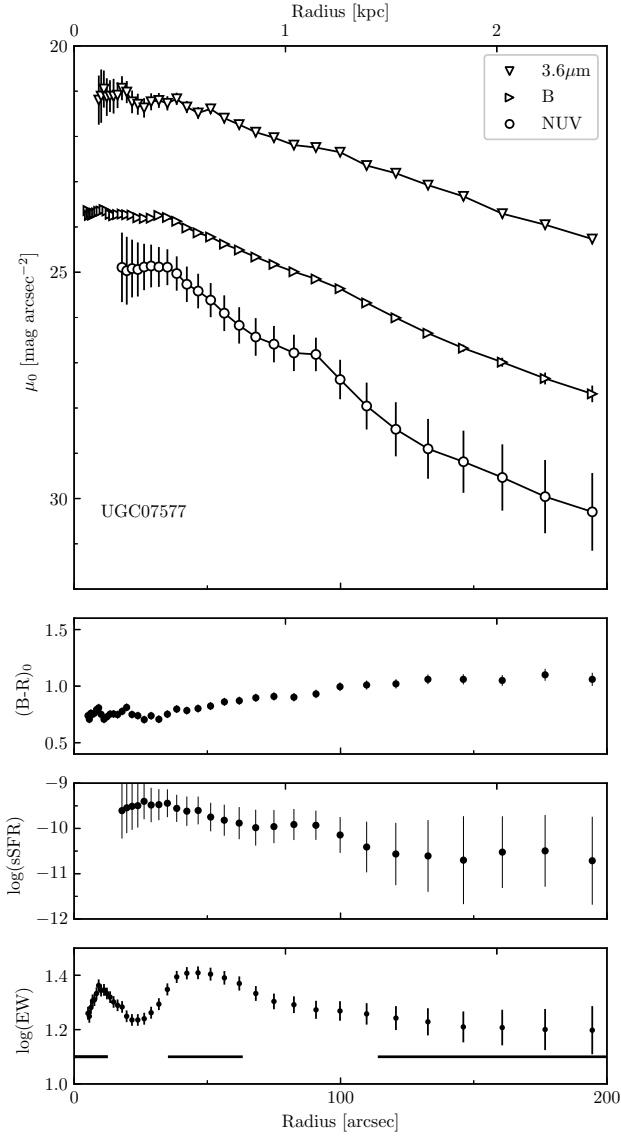


**Figure A34.** UGC 07577 : Panels same as Figure A1.

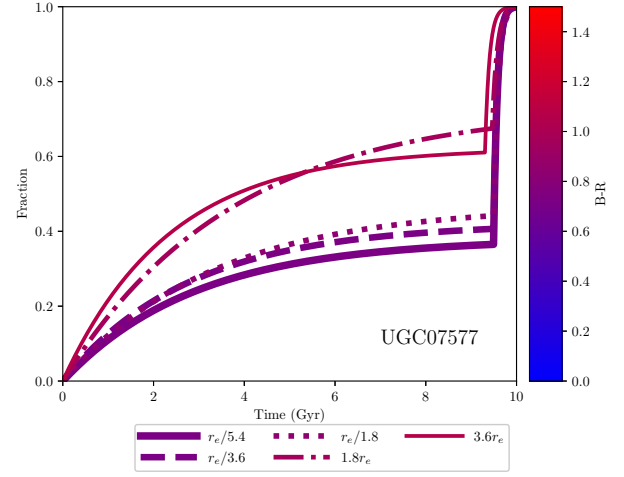


**Figure A35.** UGC 07577 : Plot same as Figure A2.

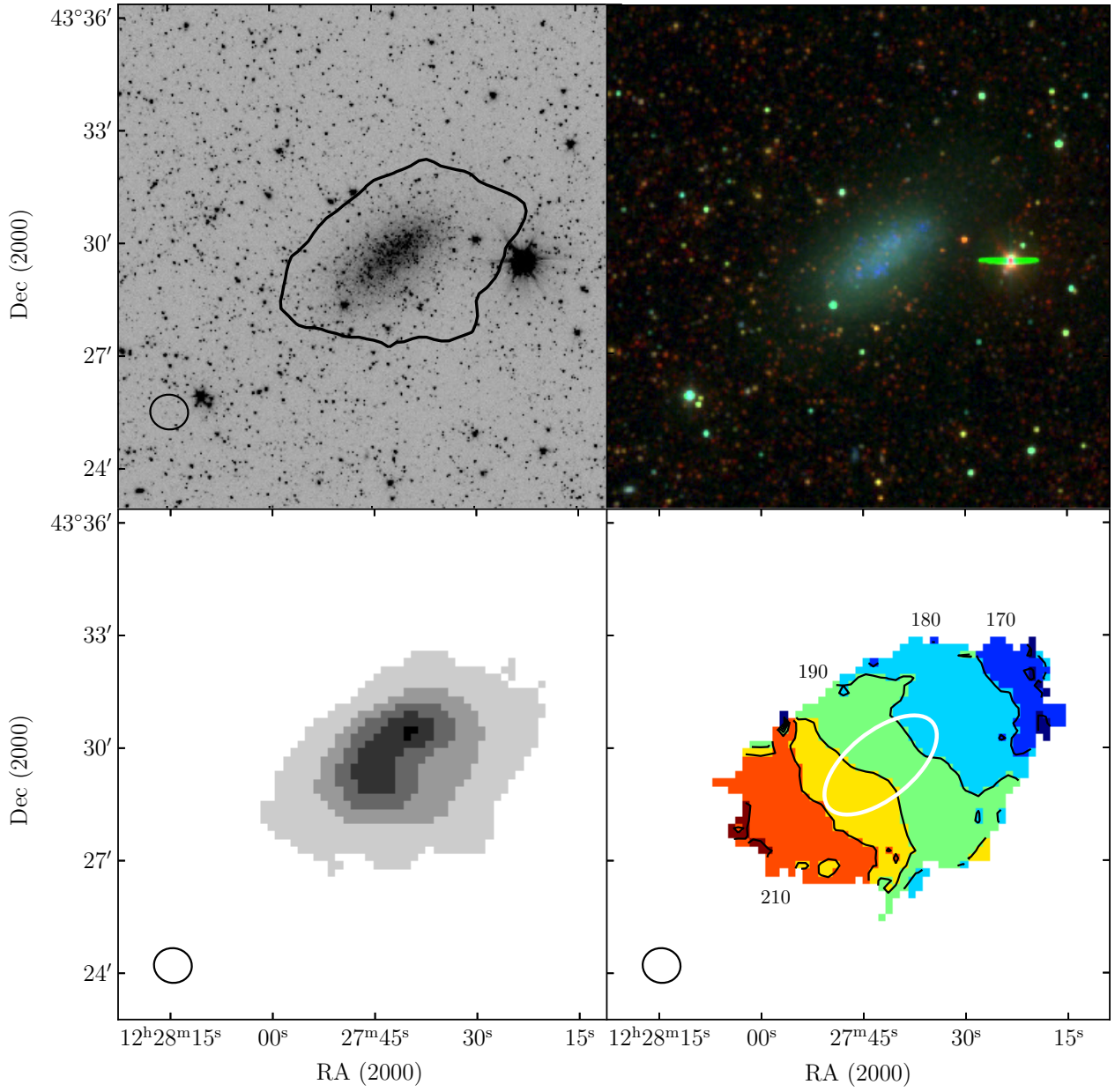


**Figure A36.** UGC 07577 : Panels same as Figure A3.

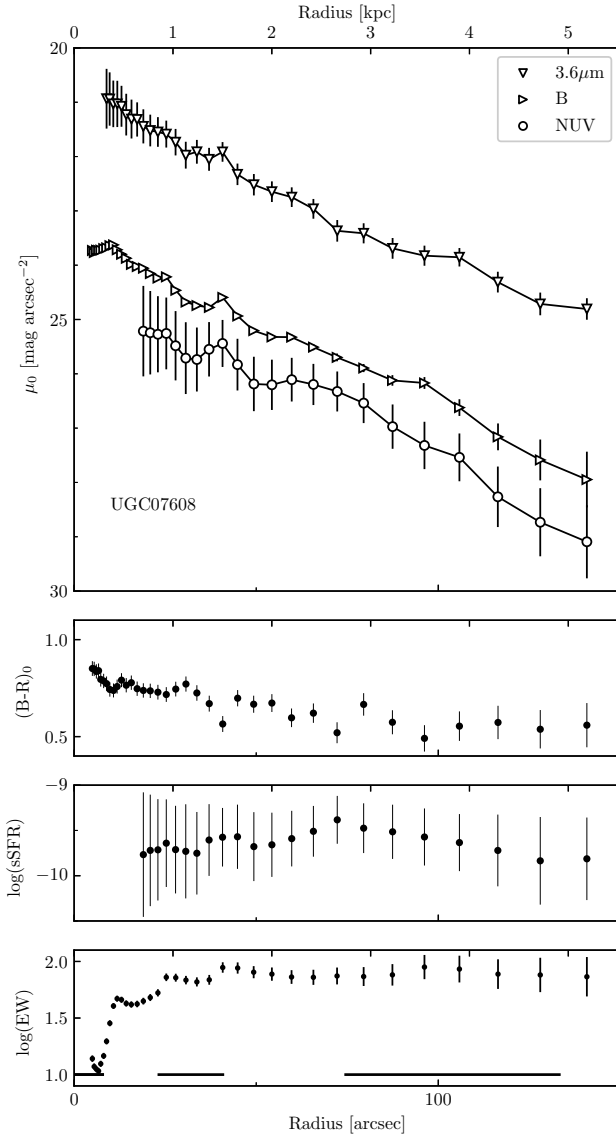


**Figure A37.** UGC 07608 : Panels same as Figure A1.

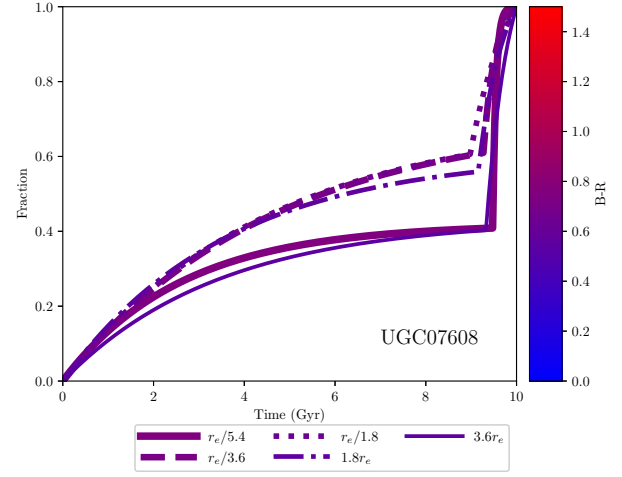


**Figure A38.** UGC 07608 : Plot same as Figure A2.

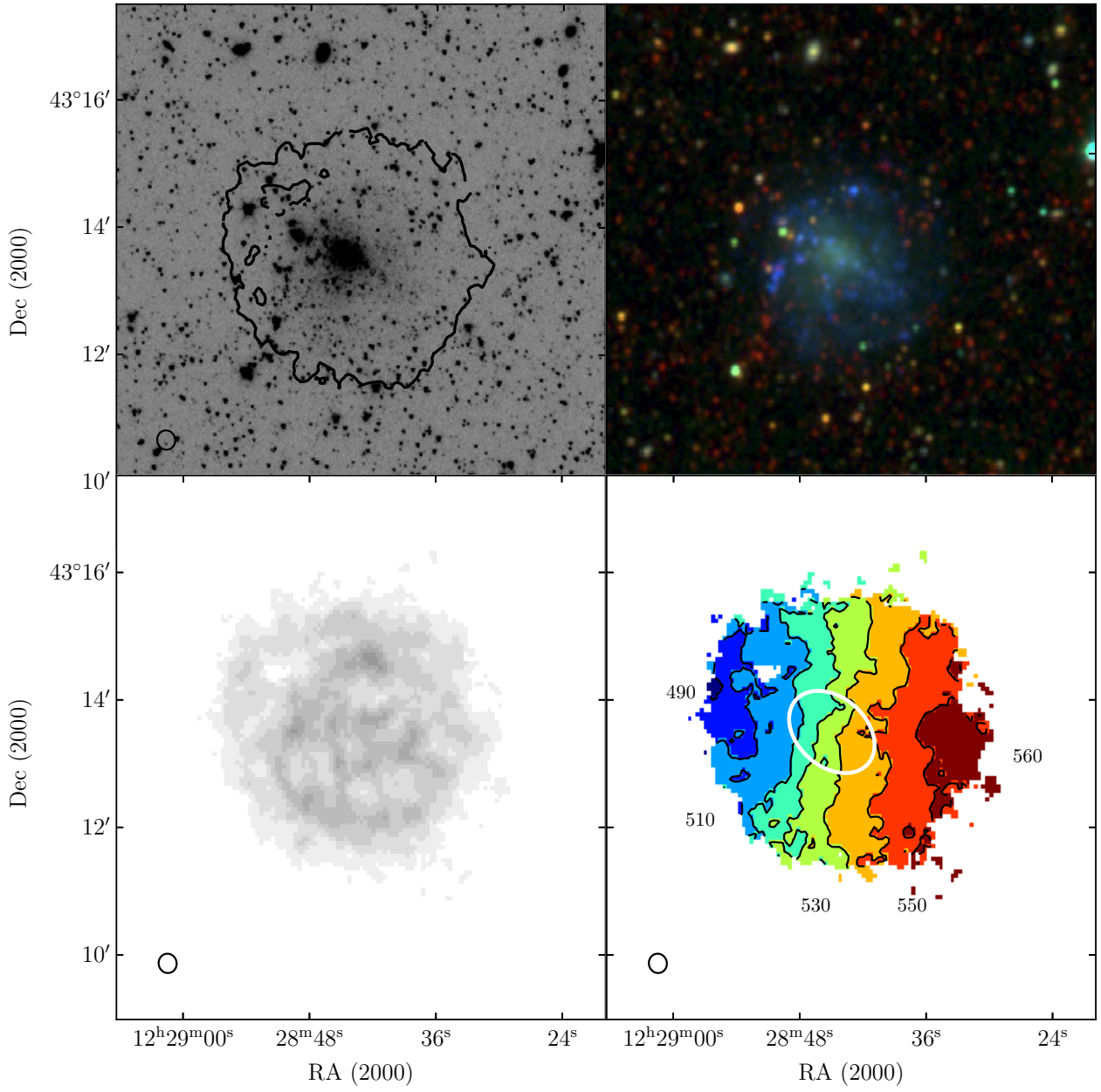


**Figure A39.** UGC 07608 : Panels same as Figure A3.



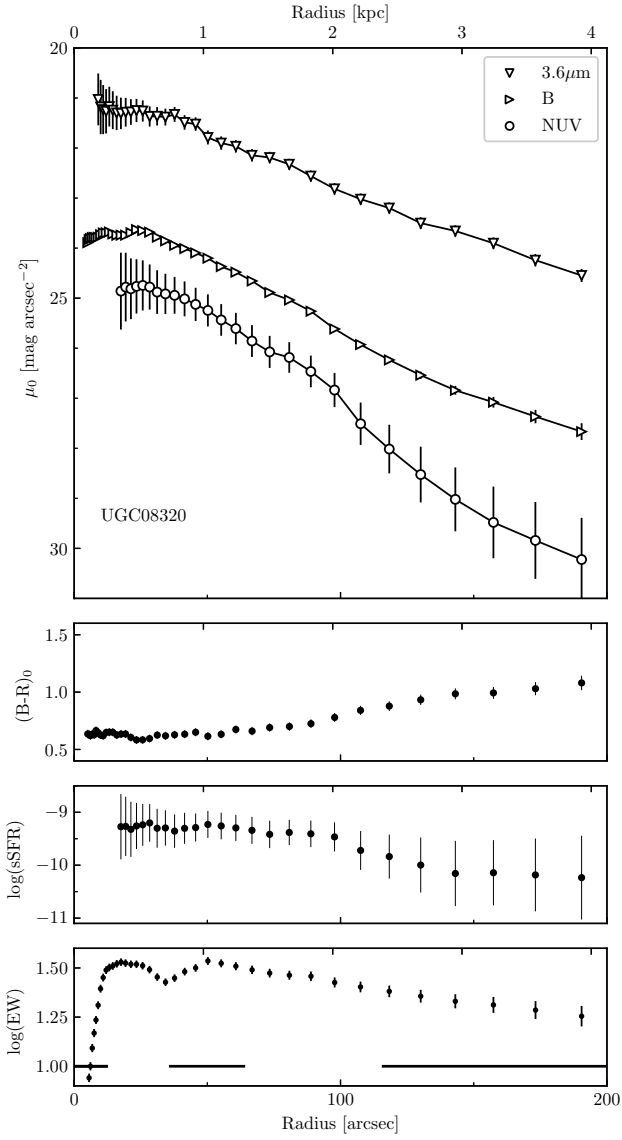


**Figure A40.** UGC 08320 : Panels same as Figure A1.

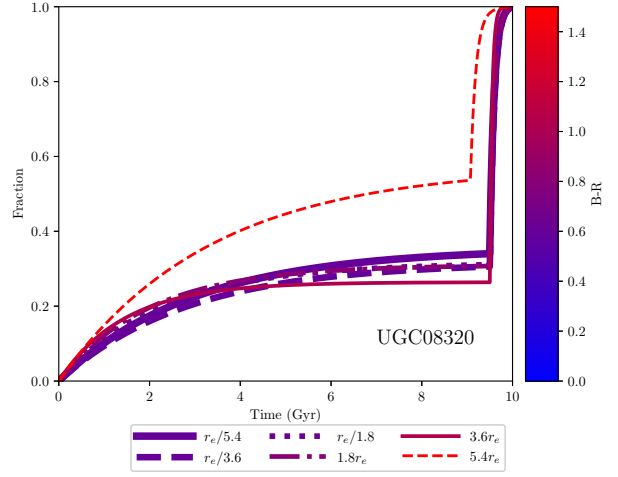


**Figure A41.** UGC 08320 : Plot same as Figure A2.

This paper has been typeset from a  $\text{\LaTeX}$  file prepared by the author.

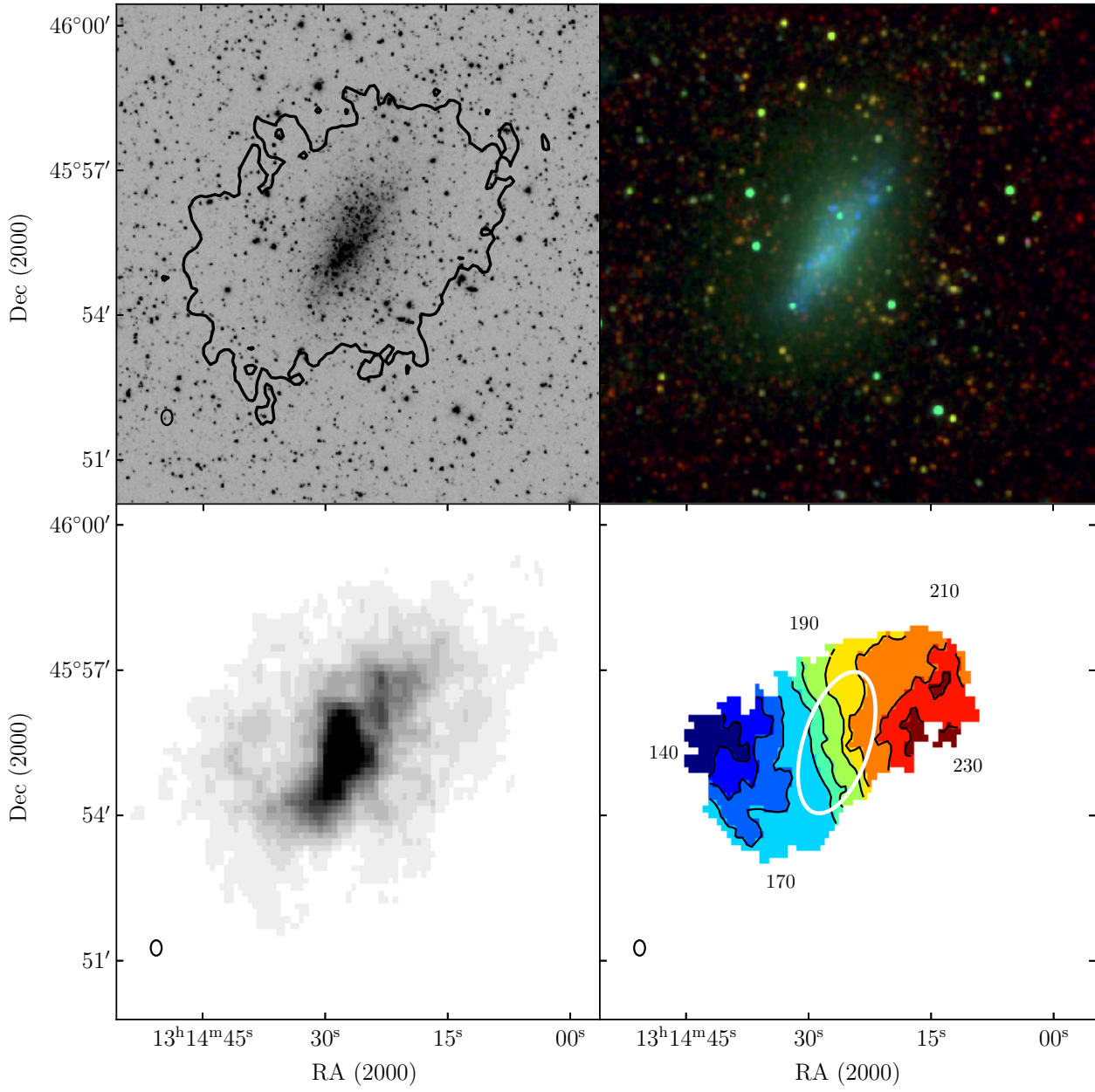


**Figure A42.** UGC 08320 : Panels same as Figure A3.